Machine-learning and mechanistic modeling of primary and metastatic breast cancer growth after neoadjuvant targeted therapy

Sébastien Benzekry, Michalis Mastri, Chiara Nicolò, John Ebos

Machine-learning and mechanistic modeling of metastatic breast cancer after neoadjuvant treatment

Sebastien Benzekry[1*], Michalis Mastri[2], Chiara Nicolò[3] and John M.L. Ebos[2,4]

1. *Computational Pharmacology and Clinical Oncology (COMPO), Inria Sophia Antipolis–Méditerranée, Cancer Research Center of Marseille, Inserm UMR1068, CNRS UMR7258, Aix Marseille University UM105, Marseille, France*

2. *Department of Cancer Genetics and Genomics, Roswell Park Comprehensive Cancer Center, Buffalo, New York, USA.*

3. *InSilicoTrials Technologies S.P.A, Riva Grumula , , Trieste, Italy.*

4. *Department of Medicine, Roswell Park Comprehensive Cancer Center, Buffalo, New York, USA.*

* sebastien.benzekry@inria.fr

Running title: Mathematical modeling of metastasis after neoadjuvant therapy

Conflict of interest: The authors declare no potential conflicts of interest

Abstract

Clinical trials involving systemic neoadjuvant treatments in breast cancer aim to shrink tumors before surgery while simultaneously allowing for controlled evaluation of biomarkers, toxicity, and suppression of distant (occult) metastatic disease. Yet neoadjuvant clinical trials are rarely preceded by preclinical testing involving neoadjuvant treatment, surgery, and post-surgery monitoring of the disease. Here we used a mouse model of spontaneous metastasis occurring after surgical removal of orthotopically implanted primary tumors to develop a predictive mathematical model of neoadjuvant treatment response to sunitinib, a receptor tyrosine kinase inhibitor (RTKI). Treatment outcomes were used to validate a novel mathematical kinetics-pharmacodynamics model predictive of perioperative disease progression. Longitudinal measurements of presurgical primary tumor size and postsurgical metastatic burden were compiled using 128 mice receiving variable neoadjuvant treatment doses and schedules (released publicly at https://zenodo.org/records/10607753). A non-linear mixed-effects modeling approach quantified inter-animal variabilities in metastatic dynamics and survival, and machine-learning algorithms were applied to investigate the significance of several biomarkers at resection as predictors of individual kinetics. Biomarkers included circulating tumor- and immune-based cells (i.e., circulating tumor cells and myeloid-derived suppressor cells) as well as immunohistochemical tumor proteins (i.e., CD31 and Ki67). Our computational simulations show that neoadjuvant RTKI treatment inhibits primary tumor growth but has little efficacy in preventing (micro)-metastatic disease progression after surgery and treatment cessation. Machine learning algorithms that included support vector machines, random forests, and artificial neural networks, confirmed a lack of definitive biomarkers, which shows the value of preclinical modeling studies to identify potential failures that should be avoided clinically.

Author summary: Using simulations from a mechanistic mathematical model compared with preclinical data from surgical metastasis models, we found that anti-tumor effects of neoadjuvant receptor tyrosine kinase inhibitor treatment can differ between the primary tumor and metastases in the perioperative setting. Model simulations with variable drug doses and scheduling of neoadjuvant treatment revealed a contrasting impact on initial primary tumor debulking and metastatic outcomes long after treatment has stopped and the primary tumor has been surgically removed. Using machine-learning algorithms, we identified the limited power of several circulating cellular and molecular biomarkers in predicting metastatic outcomes, uncovering a potential fast-track strategy for assessing future clinical biomarkers by pairing patient studies with identical studies in mice.

Introduction

Neoadjuvant trials in breast cancer (BC) patients involve the administration of systemic treatment for a limited period to treat (and reduce) localized primary tumors before surgery [1]. Neoadjuvant trials provide several advantages to assist in novel drug development and translational research. They can be faster to conduct (than, e.g., adjuvant trials), require fewer patients, offer the potential for controlled assessment of biological tissue for novel biomarker development, and critically, can potentially limit distant (often occult) metastatic lesions to delay disease recurrence long after treatment has ended [1,2]. Yet there are surprisingly few studies that precede neoadjuvant trial design to offer predictive guides to validate drug efficacy, biomarkers, or possible outcomes. In this regard, *in silico* (mathematical) modeling and preclinical *in vivo* testing can be useful. However, mathematical modeling most often occurs as post-hoc analysis in BC trials, and studies in mice rarely include clinically relevant systems that capture the complexity of surgical impact on primary/metastatic growth to offer rationalized inclusion of biomarkers in trial design [3].

To address this gap, here we describe a mathematical modeling framework of neoadjuvant therapy, using a combination of preclinical *in vivo* and *in silico* data to provide a predictive platform for treatment outcomes. This extends from our prior work that validated a semi-mechanistic model comparing localized 'primary' tumor growth with the growth of spontaneous metastatic disease that occurred after surgery in mouse models of BC [4]. We used 'ortho-surgical' models (i.e., orthotopic implantation followed by surgical tumor resection) to show that inter-individual variability in the kinetics of metastatic growth could be captured by the distribution of a critical parameter of metastatic aggressiveness.

In the current study, we examined neoadjuvant treatment with sunitinib, a molecular targeted tyrosine inhibitor (TKI) that can block angiogenesis-associated vascular endothelial growth factor receptors (VEGFRs) along with several other regulators of metastasis [5]. Using a VEGFR TKI had several advantages. First, they have a short half-life, which allowed us to confine treatment effects to the presurgical period and incorporate multiple variations of treatment dosing, days treated, and time of resection after initial tumor implantation in mice [6]. Second, VEGFR TKIs have shown mixed effects in the perioperative setting in BC [7]. While the addition of neoadjuvant sunitinib to chemotherapy improved pathologic complete response rates, long-term results have been more contrasted, with no disease-free survival benefit and either none [8] or some [9] overall benefit. As a monotherapy, we and others have demonstrated that robust inhibition of primary tumor growth does not always translate into inhibition of metastasis post-surgically nor improvement in survival [10,11]. However, the mechanistic determinants of these counter-intuitive findings remain elusive. In our experimental model, we measured multiple cellular and molecular biomarkers at surgery. Adding here neoadjuvant treatment to our mathematical modeling framework allowed us to 1) formulate and test mechanistic hypotheses about differential effects on primary versus secondary disease, 2) evaluate the impact of biomarkers on metastatic development and 3) investigate the impact of modulating dosing regimen.

For 2), we use machine learning to investigate the predictive power of biomarkers on the mechanistic parameters of our neoadjuvant mathematical metastatic model. Machine learning (ML) coupled with mechanistic modeling – an approach that we term

47 ‘mechanistic learning’ [12,13] – can screen biomarkers with translational potential and
48 establish predictive models [14]. In contrast to classical statistical analysis, ML consists
49 in designing models with predictive performances as metrics of success, instead of
50 inference properties. It also makes use of nonlinear models such as regression trees
51 or artificial neural networks [15].
52

Materials and Methods

Ethics Statement

Animal studies were performed in strict accordance with the recommendations in the Guide for Care and Use of Laboratory Animals of the National Institute of Health and according to guidelines of the Institutional Animal Care and Use Committee at Roswell Park Comprehensive Cancer Center (protocol: 1227M, PI: John M.L. Ebos).

Data and code availability

The data is publicly available at https://zenodo.org/records/10607753 [16]. The code used to perform the analysis and generate the figures is also publicly available at https://gitlab.inria.fr/benzekry/metamats.burden.treatment. We also provide a software heritage identifier permalink for a code snapshot at the time of publication, ensuring that any future modifications to the code won't compromise the reproducibility of the results [17].

Experimental system

Cell lines

The human LM2-4^{LUC+} cells are a luciferase-expressing metastatic variant of the MDA-MB-231 breast cancer cell line derived after multiple rounds of *in vivo* lung metastasis selection in mice, as previously described [5]. LM2-4^{LUC+} were maintained in DMEM (Corning cellgro; 10-013-CV) supplemented with 5% v/v FBS (Corning cellgro; 35-010-CV), in a humidified incubator at 37oC and 5% CO2. The cell line was authenticated by STR profiling (DDC Medical, USA).

Drug and doses used

Sunitinib malate (SU11248; Sutent, Pfizer) is a molecular receptor tyrosine kinase inhibitor (RTKI) that can block angiogenesis-associated vascular endothelial growth factor receptors (VEGFRs) along with several other regulators of metastasis [18]. The molecule was suspended in a vehicle formulation that contained carboxymethylcellulose sodium (USP, 0.5% w/v), NaCl (USP, 1.8% w/v), Tween-80 (NF, 0.4% w/v), benzyl alcohol (NF, 0.9% w/v), and reverse osmosis deionized water (added to final volume), which was then adjusted to pH 6. The drug was administered at 60 or 120 mg/kg/day orally by gavage as previously described [10,19]. The treatment window used in all neoadjuvant studies consisted of a previously optimized 14-day period before surgery [10]. Within these 14 days, daily sunitinib (Su) treatment was given either at 60 mg/kg/day (for 3, 7, or 14 days followed by vehicle for 11, 7, or 0 days, respectively), or at 120 mg/kg/day for 3 days followed by 60 mg/kg/day for 0, 4, 8, or 11 days, and vehicle for 11, 7, 3, or 0 days, respectively. An example of an abbreviation in the text includes ‘Su60(14D)’, which means ‘sunitinib at 60mg/kg/day for 14 days. Schematics for all studies are shown in S1 Table. Mice treated daily with vehicle for 14 days were used as controls. Detailed analysis and comparisons of these treatment regimens are described in a companion study evaluating treatment breaks on metastatic disease.

Ortho-surgical model of metastasis

Implantations*:* Experimental methodology was extended from previous work using a xenograft animal model of breast cancer spontaneous metastasis that includes orthotopic implantation followed by surgical resection of a primary tumor (termed 'ortho-surgical') [4]. Briefly, LM2-4^{LUC+}(1 x 10^6 cells in 100µl DMEM) were orthotopically implanted into the right inguinal mammary fat pad (right flank) of 6- to 8-week-old female SCID mice, as described previously [4,10,19]. Primary tumor **(PT)** burden was monitored with Vernier calipers using the formula width^2(length x 0.5) and bioluminescence imaging (BLI) [4,10,19]. Neoadjuvant treatments started 14 days before primary tumors were surgically removed at a timepoint (34-38 days post-implantation) previously optimized for maximal distant metastatic seeding but minimal localized invasion [4,10]. The surgeries were planned at specific time points post-implantation to avoid invasion of the primary tumor into the skin or peritoneal wall, ensuring that metastatic progression had proceeded and minimizing the possibility of surgical cure [4,10]. Postsurgical metastatic burden **(**MB**)** was assessed by BLI and overall survival was monitored based on signs of end-stage disease as previously described [4,10].

Exclusion criteria*:* Two scenarios represented instances where animals were excluded from treatment studies. First, if complete removal of the primary tumor was not surgically feasible because of local invasion or evidence of advanced metastatic spread [4,19]. Second, if no primary or metastatic tumor was ever detected by BLI or visual assessment it was assumed there was lack of tumor-take upon implantation [4,10].

Randomization*:* Before treatment initiation animals were randomized by primary tumor size assessed by Vernier calipers to avoid any false results due to unequal tumor burden between groups [20].

Biomarkers

Flow cytometry

Peripheral blood was collected in tubes containing lithium heparin (BD Biosciences; 365965) by orbital bleeding one day before surgical tumor resection. Non-specific binding was blocked with normal mouse IgG (Invitrogen; 10400C) incubated with whole blood, followed by incubation with an antibody mix. After staining, cells were fixed in a lyse/fix solution (BD Biosciences; 558049), while red blood cells were lysed. Samples were analyzed with a LSR II flow cytometer (Becton Dickinson), while data were acquired with FACSDiva software (Becton Dickinson) and analyzed with FCS Express 6 (DeNovo software).

Circulating tumor cells (CTC)

The antibody mix for CTC detection of human CTCs in animal models contained a rat anti-mouse CD45 (30-F11) antibody conjugated to PE (Biolegend; 103106) and mouse anti-human HLA conjugated to AlexaFluor 647 (Biolegend; 311416). CD45 staining with a rat anti-mouse CD45 conjugated to FITC (Invitrogen; MCD4501) was used to eliminate any mouse blood cells, whereas human HLA was used to identify CTC (human LM2-4^{LUC+}). For positive control, LM2-4^{LUC+} cells were trypsinized, washed with PBS, and stained for both CD45 and HLA. LM2-4^{LUC+} cells were used to define the CTC gate.

Circulating myeloid-derived suppressor cells (MDSC)

The antibody mix for detection of MDSCs contained a rat anti-mouse CD45 (30-F11) antibody conjugated to PE (Biolegend; 103106), a rat anti-mouse Ly-6G/Ly-6C (Gr1)

(RB6-8C5) antibody conjugated to PE-Cy7 (BD Pharmingen; 552985), and a rat anti-mouse CD11b (M1/70) antibody conjugated to eFluor450 (eBioscience; 48-0112). Mouse CD45 staining was used to select only leukocytes, and CD11b and Gr1 were used to define the granulocytic and monocytic MDSC.

Immunofluorescence

Resected tumors were frozen on dry ice in a cryo-embedding compound (Ted Pella, Inc; 27300), sectioned, and fixed in a 3:1 mixture of acetone:ethanol. Non-specific binding was blocked with 2% BSA in PBS, followed by staining with an antibody mix containing rabbit anti-mouse Ki67 antibody (Cell Signaling Technologies; 12202) and rat anti-mouse CD31 antibody (Dianova; DIA-310). Detection of primary antibodies was achieved using FITC conjugated goat anti-rabbit IgG (BD Pharmingen; 554020) and Cy3 conjugated goat anti-rat IgG (Invitrogen; A10522). Samples were counterstained with DAPI (Vector; H-1500) and mounted with a hard-set mounting medium for fluorescence. Random images from each section were obtained with a Zeiss AxioImager A2 epifluorescence microscope at 200x magnification, and analyzed with ImageJ. CD31+ cells (% area) and Ki67+ cells (% cells) were quantified automatically using macro functions, whereas Ki67+/CD31+ cells (proliferating endothelial cells) were quantified manually.

Mechanistic modeling of untreated pre- and post-surgical metastatic development

For untreated animals, we previously validated a mechanistic model for the description of pre-surgical primary tumor and post-surgical metastasis kinetics in the ortho-surgical LM2-4^{LUC+} animal model [4]. Briefly, metastatic development is decomposed into two main processes: growth and dissemination.

Growth of the PT and metastases follow the Gomp-Exp model [21]:

$$g_p(v) = g(v) = \min\left(\lambda v, \left(\alpha - \beta \ln\left(\frac{v}{V_0}\right)\right) v\right),$$

where g_p and g denote the growth rates of the primary and secondary tumors, respectively. Parameter λ limits the Gompertz growth rate to avoid unrealistically fast kinetics for small sizes and is given by the *in vitro* proliferation rate, assessed previously [4]. Parameters α and β are the Gompertz parameters, and V_0 is the size of one cell (in units of mm^3 for the PT, and photons/seconds for the metastases). The PT volume, $V_p(t)$ thus solves

$$\begin{cases} \frac{dV_p}{dt} = g_p(V_p) \\ V_p(t=0) = V_i, \end{cases}$$

with V_i the volume corresponding to the number of cells injected (= 1 mm^3 based on the conversion rule 1 mm^3 $\simeq$ 10^6 cells [22]).

Dissemination occurs at the following volume-dependent rate [4]:

$$d(V_p) = \mu V_p,$$

where parameter μ can be interpreted as the daily probability that a cell from the PT successfully establishes a metastasis [4].

The metastatic process was described through a function $\rho(t,v)$ representing the distribution of metastatic tumors with size v at time t. It solves the following initial boundary value problem [23]:

$$\begin{cases} \partial_t \rho(t,v) + \partial_v\big(g(v)\rho(t,v)\big) = 0, & t \in (0,+\infty),\ v \in (V_0,+\infty) \\ g(t,V_0)\rho(t,V_0) = d\left(V_p(t)\right), & t \in (0,+\infty) \\ \rho(0,v) = 0, & v \in (V_0,+\infty) \end{cases}$$

The first equation derives from a balance equation on the number of metastases; the second equation is a boundary condition for the rate of newly created metastases; the third equation is the initial condition (no metastases exist at the initial time).

The MB at time t was then given by

$$M(t) = \int_{V_0}^{+\infty} v\rho(t,v)dv = \int_0^t d\left(V_p(t-s)\right)V(s)ds\,,$$

which can be solved efficiently through the use of a fast Fourier transform algorithm [24]. In the previous equation, $V(s)$ represents the volume reached by a metastatic tumor after time s from its birth, when growing with growth rate g.

Heuristic modeling of neoadjuvant therapy (NAT)

In the first phase of investigations (Fig 1), we leveraged the previously identified parameters of our model for untreated metastatic development [4]. NAT was grossly modeled by simply setting either g_p (Scenario A) or g_p and g (Scenario B) to zero, during NAT. This allowed us to perform pure predictions that did not require any parameter fitting to the data.

Figure 1: Mathematical modeling reveals differential effects of neoadjuvant sunitinib treatment on primary tumor and metastatic growth.

(A) Schematic of the study. Data from an ortho-surgical, human xenograft animal model of neoadjuvant sunitinib breast cancer treatment were fitted using a mixed-effects statistical framework. This provided calibrated parameters for each animal. Machine learning algorithms were used to assess the predictive power of molecular and cellular biomarkers to predict the metastatic dissemination parameter μ and quantify metastatic aggressiveness.

(B) Schematic of tested hypotheses of the effect of neoadjuvant sunitinib Tx on primary tumor and metastatic growth and dissemination through mechanistic mathematical modeling. Scenario A = growth arrest on both primary and secondary tumors. Scenario B = growth arrest on primary tumor only.

(C) Predicted simulations of Scenarios A and B using parameters calibrated from a previous study involving untreated (vehicle) animals only [4]. Data plotted here (LM2-4^{LUC+} bioluminescent human breast cancer cells orthotopically injected in mice) was not used to estimate the model parameters.

*Tx, treatment; PT, primary tumor; MB, metastatic burden. *See methods for additional details on animal experiments, treatment dose and duration, and mechanistic model. The mouse images were drawn using Biorender.*

Kinetics-pharmacodynamics modeling of NAT

Structural model

We next incorporated the effects of systemic therapy in a way that accounts for systemic concentration kinetics resulting from the drug scheduling regimen (dose and timing of administration). This new model assumes that the drug reduces the primary tumor growth rate by a term proportional to its concentration, $C(t)$ (Norton-Simon hypothesis [25]):

$$g_p^T(t,v) = g_p(v)\big(1 - k\,C(t)\big)$$

where k is a parameter of drug efficacy. As no pharmacokinetic data was available, we used a kinetics-pharmacodynamics (K-PD) approach. Namely, we considered that the drug concentration decays exponentially after each dose,

$$C(t) = \frac{1}{V_d}\sum_{i=1}^{n} D_i e^{-k_e(t-\tau_i)}\mathbb{I}_{t>\tau_i},$$

where D_i indicates the dose administered at time τ_i. The volume of distribution V_d and the elimination rate constant k_e were fixed to the values reported in [26].

Parameter identification for the K-PD model

Following previously established methodology [4], the parameters were identified from the experimental data using a nonlinear-mixed effects modeling approach [27]. Briefly, this consists of modeling inter-animal variability by assuming a parametric distribution for the model parameters. All individual PT and MB longitudinal data could then be pooled together in a population model, whose parameters were estimated by likelihood maximization [27]. In mathematical terms, if y_j^i denotes the observation (primary tumor size or metastatic burden) in animal i at time t_j^i and $f(t_j^i;\theta^i)$ denotes the model prediction in an animal with parameter set $\theta^i = (\alpha^i, \beta^i, k^i, \mu^i)$, we log-transformed the data and assumed a proportional error model. The statistical observation model thus writes:

$$\ln y_j^i = \ln\Big(f\big(t_j^i;\theta^i\big)\Big)\big(1+\bar{\sigma}\varepsilon_j^i\big),$$
$$\ln(\theta^i) = \ln\big(\theta_{pop}\big) + \eta^i, \quad \eta^i \sim \mathcal{N}(0,\Omega),$$

where $\varepsilon_j^i \sim \mathcal{N}(0,1)$ is a Gaussian noise for measurement error. The parameters θ_{pop} and Ω characterize the entire population. The observed data were log-transformed and a proportional error model was used, that is

$$\ln y_j^i = \ln\Big(f\big(t_j^i;\theta^i\big)\Big)\big(1+\bar{\sigma}\varepsilon_j^i\big).$$

For the vector of individual parameters, a log-normal distribution with full covariance matrix was assumed. Maximum likelihood estimates of the population parameters were obtained using the Stochastic Approximation of Expectation-Maximization (SAEM) algorithm implemented in the *nlmefitsa* Matlab function [28]. PT and MB data were fitted simultaneously for vehicle and sunitinib-treated animals. Visual predictive checks (VPC), individual fits and standard diagnostic graphical tools based on individual parameters were used to evaluate the adequacy of the different model components.

Definition of metastatic relapse

To define a time of metastatic relapse, we aimed to mimic the human situation in which 30% of breast cancer patients with localized disease undergo metastatic relapse [29]. Therefore, we defined a MB relapse threshold to be the 30th percentile of the control population MB at 85 days (considered to be an approximation of long-term), i.e. 6.322 x 10^8 cells. This threshold then allowed us to compute the percent of subjects having metastatic relapse in the virtual populations, under varying NAT scheduling regimens.

Machine learning algorithms

Effects of covariates on the model parameters were assessed using linear regression and several machine learning regression techniques (partial least squares, artificial neural networks, support vector machines and random forest models) using the R caret package [30,31]. Except for the random forest models, data were centered and scaled before modeling. Tuning parameter values of the regression models were selected to minimize the root mean squared error (RMSE) using five replicates of a 10-fold cross-validation. If θ^i are the true values and $\hat{\theta}^i$ the predicted ones, the RMSE is defined by:

$$RMSE = \sqrt{\frac{\sum_i \left|\hat{\theta}^i - \theta^i\right|^2}{N}}.$$

Results

In vivo/in silico modeling of neoadjuvant therapy (NAT) suggests limited effect on metastasis growth

The previously reported "paradoxical" observation of a differential effect of NAT on the pre-surgical primary tumor (PT) and post-surgical metastatic burden (MB) [10,11] could result from two phenomena that are mixed in MB quantification: 1) metastatic growth suppression and 2) reduction of metastatic spread as a consequence of primary tumor size reduction. To disentangle the two, we used quantitative mathematical modeling to compare biological hypotheses to the data. (Schematic shown in Fig 1A; see Methods for the mathematical model definition). Since our previously developed model did not account for treatment [4], we first used a heuristic approach to model NAT. In 'scenario A', NAT would have growth-arresting effects on both PT and MB, while in 'scenario B' NAT would have an effect only on PT (schematically shown in Fig 1B). This way, we could use previously calibrated parameters[4], and only set either both growth rates g_p and g (Scenario 'A') or g_p only (Scenario 'B') to zero during NAT. This allowed us to make predictions without relying on data fitting. Scenario 'A' clearly failed to describe the data (Figs 1C and S1), whereas Scenario 'B' interestingly demonstrated good accuracy (Figs 1C and S1). These results demonstrate a differential effect of NAT on the growth of primary and secondary tumors and suggest that a mathematical model of NAT in our breast cancer ortho-surgical animal model should not include an anti-growth effect on metastasis.

Calibration and validation of a kinetics-pharmacodynamics (K-PD) model for NAT

Subsequently, to further link dose and scheduling to response, we developed a K-PD metastatic model of NAT using a defined treatment window (14 days) containing multiple treatment periods (3, 7, 11, 14 days), doses (60 mg and 120 mg), and time of surgery after tumor implantation (day 34 or 38) (see S1 Table and methods for details). Following our findings above, we only adapted the PT growth rate g_p from [4], using the Norton-Simon hypothesis for the PT anti-growth effect of NAT [25]. Estimates of the model parameters are reported in Table 1 and demonstrate high practical identifiability (relative standard error ≤ 17%), likely owing to the large number of subjects in the population fit. In addition, the estimate of the proportional error parameter $\bar{\sigma}$ (3.91%) indicated accurate goodness-of-fit.

Parameter (Unit)	Meaning	Median value	CV (%)	r.s.e. (%)
μ (cell^{-1}.day^{-1})	Dissemination coefficient	2.12e-11	1.48e+03	17.3
α (day^{-1})	Gompertzian growth parameter	1.94	18.1	2
β (day^{-1})	Gompertzian growth parameter	0.0911	19.7	2.21

λ (day^{-1})	In vitro proliferation rate	0.837 (fixed)	-	-
k (L/mg)	Drug efficacy	0.446	32.1	6.34
k_e (day^{-1})	Drug elimination rate	3.26 (fixed)	-	-
V_d (L)	Drug volume of distribution	12 (fixed)	-	-
$\bar{\sigma}$ (%)	Error parameter	3.91	-	-

Table 1: Parameter estimates of the metastatic and survival models obtained by likelihood maximization via the SAEM algorithm.

Abbreviations: CV, coefficient of variation computed as the ratio of the standard deviation and the median of the estimated parameter distribution; r.s.e., residual standard error.

Confirming our previous results [4], the metastatic potential parameter μ was found to vary significantly amongst individuals (largest coefficient of variation). Visual predictive checks for both the vehicle group and treated groups demonstrated accurate goodness-of-fit both at the population (Figs 2A and S2) and individual (Figs 2B and S3) levels. In addition, model predictions in independent data sets unused for parameter calibration, with distinct times of surgery (day 38 versus day 34) and drug regimens, were in good agreement with the data (S4 Fig). Further model diagnostic plots demonstrated no clear misspecification of the structural and residual error model (S5 Fig). Distributions of the empirical Bayes estimates were in agreement with the theoretical distributions defined in the statistical model (S6 Fig). Moreover, the η-shrinkage was less than 20% for each parameter, meaning that the individual parameter estimates and the diagnostic tools based on them can be considered reliable [32]. Finally, correlations found between the estimated random effects (S7 Fig) confirmed the appropriateness of a full covariance matrix in the assumed distribution of the individual parameters.

Fig 2: Calibration and validation of a kinetics-pharmacodynamics (K-PD) mathematical model for neoadjuvant sunitinib treatment effect on pre- and post-surgical tumor growth

Pre- and postsurgical growth of LM2-4^{LUC+} human metastatic breast carcinomas were measured in multiple groups involving different neoadjuvant treatment modalities (doses and durations). The mathematical model was fitted to the experimental data using a mixed-effects population approach (n=104 animals in total).

(A) Comparison of the simulated model population distribution (visual predictive check) for vehicle and neoadjuvant sunitinib treatment (60mg/kg/day) 14 days before surgery.

(B) Examples of individual dynamics.

Tx, treatment; PT, primary tumor; MB, metastatic burden.

Together, these results show the validity of our mathematical model to simulate PT and MB kinetics under a wide range of NAT administration regimens, which can thus be employed to explore *in silico* the quantitative impact of possible NAT schedules.

Simulations of NAT duration reveal a different impact on PT size reduction and metastasis-free survival

The overall impact of NAT is the combination of i): PT debulking (which in turn reduces metastatic spread from the PT), and ii) an increased risk of metastatic relapse due to delayed removal of the PT. To quantify the impact of NAT duration on these two opposite aspects, we ran simulations of our calibrated model for NAT durations ranging between 0 to 18 days. The NAT initiation time was fixed to 27 days, assumed to be the time of detection of the primary tumor. The resection time fixed was then varied from 27 to 45 days. Three dose levels were simulated (60, 120, and 240 mg/kg, see Fig 3). First, using only the typical population estimates of the parameters (median individual), we found an important increase in postsurgical MB for long NAT: final values ranged from 2.73×10^8 to 7.52×10^8 cells for NAT durations from 0 to 18 days (176% increase), respectively, at the 60 mg/kg dose level (Fig 3A). This is consistent with our model where NAT does not affect metastatic growth, thus delaying surgery can only increase MB. This was less important in higher dose levels (125% and 48.5% increases for 120 mg/kg and 240 mg/kg, respectively). To study the impact of inter-individual variability, we leveraged our mixed-effects framework to perform population simulations and quantify the outcome. Namely, we simulated 1000 virtual individuals and recorded the percent changes in PT size at the end of NAT. Fig 3B shows the resulting median PT percent changes, together with an area covering 80% of the population. In addition, we calculated a risk of metastatic relapse from the resulting simulation of MB kinetics (see Methods), which is depicted as the circled line in Fig 3B.

Fig 3: Simulations of varying neoadjuvant treatment duration quantify contrasted impact on primary tumor size reduction and risk of metastatic relapse

Using model parameters calibrated from data of our ortho-surgical animal model of breast cancer neoadjuvant targeted treatment, simulations were conducted for treatment durations varying between 0 (light color) and 18 (dark color) days, for three dose levels (60 mg/kg, 120 mg/kg and 240 mg/kg).

(A) Predicted simulations of pre-surgical primary tumor and post-surgical metastatic kinetics. Note: for the 240 mg/kg plot, the metastatic burden growth curves with the three longest treatment durations are superimposed and not distinguishable.

(B) Population-level predictions of final primary tumor size (solid line and grey area) and probability of metastatic relapse as functions of the duration of neoadjuvant treatment, which delays surgical removal of the primary tumor (circled line). Inter-individual variability simulated from the population distribution of the parameters learned from the data (n = 1000 virtual subjects).

Tx, treatment; PT, primary tumor; MB, metastatic burden

For 60 mg/kg and 120 mg/kg doses, the metastatic relapse risk was predicted to increase drastically when delaying PT removal too long. However, for a 240 mg/kg dose (or for virtual subjects with increased sensitivity to treatment), the increase in metastatic relapse risk was more moderate, since a prolonged NAT was associated with a large decrease in the PT size that translated into a significant reduction of metastatic seeding. Together, these results illustrate how our mathematical model, informed by preclinical data, can provide informative quantitative simulations of the impact of treatment

schedules. Our findings suggest a moderate to detrimental impact of long sunitinib NAT at low doses.

Machine learning for prediction of the metastatic aggressiveness parameter μ from biomarkers at the time of surgery

Next, we wanted to determine whether biological parameters at the time of PT surgery but after NAT had stopped could be utilized as predictive biomarkers of postsurgical MB after treatment cessation. These biomarkers included immunohistochemical molecular protein measurements of resected PT for cell proliferation (Ki67) and blood vessel (CD31) markers in resected PTs (Fig 4A; example shown), blood-based cellular measurements of circulating myeloid-derived stromal cells (MDSCs) (Fig 4B), and circulating tumor cells (CTCs) from 66 animals (Fig 4C). We investigated whether these molecular and cellular biomarkers may parallel the observed variability in the mathematical parameters, in particular μ, whose large variability indicated potential animal subpopulations of variable metastatic potential values. We first examined correlations between biomarkers to identify potential redundancies in the data (Fig 4D). High correlations were found between Ki67 and Ki67+/CD31− ($r = 0.979$, $p < 10^{-12}$) and CTC and gMDSC ($r = 0.678$, $p = 3.95 \cdot 10^{-10}$). Next, we investigated the value of these measurements as predictive biomarkers of the mechanistic parameters: α and β capture growth kinetics, k the effect of treatment and μ metastatic dissemination. Fig 4B shows correlations between biomarkers and the parameter estimates. As the individual growth parameters α and β were highly correlated ($r = 0.997$, $p < 10^{-5}$), we used the Gompertz tumor doubling time at the volume $V_i = 1$ mm^3 to assess the impact of covariates on the tumor growth parameters. It is defined by $DT = -\frac{1}{\beta}\ln\left(\frac{\ln(2)+A}{A}\right)$, with $A = \ln\left(\frac{V_i}{V_0}\right) - \frac{\alpha}{\beta}$. A weak correlation was found between $\log(DT)$ and mMDSC levels (Fig 4E, $r = 0.275$, $p = 0.0257$). However, none of the available biomarkers was found to correlate either with μ or $\log(\mu)$ (S8 Fig). Next, partial least squares and several machine learning regression algorithms were tested to identify possible relationships between covariates and individual estimates of the metastatic potential parameter (shown in Fig 1A schematic). These included neural networks, support vector machines and random forest models [33]. Cross-validation results for the RMSE of the final regression models were compared against the intercept-only model (the constant model where predictions are the same for all animals, given by the median value in the population, μ_{pop}). As shown in Fig 4F and 4G, none of the fitted models had RMSE or R^2 significantly different from the intercept-only model. The lowest RMSE was achieved by the intercept-only model. Values of R^2 ranged from 0.133 to 0.199 across the models, with the highest value reached by the conditional random forest model. Prediction error on $\ln(\mu)$ ranged from 9.83% $\pm$ 10.7% for the best model (conditional random forests, mean $\pm$ std) to 10.6% $\pm$ 11.3% for the worse (random forests), which was not superior to the predictive power of the intercept-only model (9.71% $\pm$ 10.1%). Plotting the observed versus predicted values (S9 Fig) confirmed that the fitted algorithms were unable to explain the variability of parameter μ. Together, these results demonstrate that the biomarkers considered in this study have limited predictive power for metastatic potential as defined by μ.

Fig 4: Use of machine learning algorithms based on presurgical molecular and cellular markers to predict metastatic dissemination parameter 'μ'.

(A-C) Examples of molecular and cellular biomarker analysis.

(A) Proliferating endothelial cell identification by immunofluorescence. Tissue sections from resected tumors were stained with antibodies against mouse CD31 (red) and mouse Ki67 (green) and counterstained with DAPI (blue). Single channel and merged images are shown. Yellow arrows show proliferating endothelial cells which were counted manually.

(B) Myeloid-Derived Suppressor Cells (MDSC) quantification by flow cytometry. Whole blood was stained with anti-mouse antibodies for CD45, CD11b, and Gr1. After selection of CD45-positive cells, MDSCs were analyzed based on CD11b and Gr1 levels. Monocytic-MDSC (M-MDSC) are CD11b+/Gr1 high and granulocytic-MDSC (G-MDSC) are CD11b+/Gr1Medium. Examples of MDSC in untreated and treated animals are shown.

(**C)** CTC quantification by flow cytometry. CTCs for xenografts were identified using anti-human HLA. Blood was stained with anti-mouse CD45 and anti-human HLA. Blood and LM2-4 cell samples were overlaid in a dot plot to identify and create the gates for CTCs. Once the gates were created CTC were identified in the blood of tumor-bearing mice.

(D) Pearson correlation coefficients between biomarkers. Blue (resp. red) color indicates a positive (resp. negative) correlation, with the size of the circle being proportional to the R^2 correlation coefficient. ** $p<0.05$, ** $p<0.01$, *** $p<0.001$.*

(E) Univariate correlations between the biomarkers and the mathematical parameters. DT = doubling time.

(F) Cross-validated Root Mean Square Error (RMSE) across different machine learning regression models (see methods) utilizing the values of the biomarkers for predicting $\log(\mu)$. To assess the significance of the covariate in the models, RMSEs were compared against the value of this metric obtained using the intercept-only model. Bars are 95% confidence intervals. Shown in red is the model with the lowest RMSE. PLS = Partial Least Squares. SVM = Support Vector Machines

(G) Cross-validated R2 with 95% confidence intervals.

(H) Predictions versus observations for the conditional random forest algorithm.

Discussion

A large part of *in vivo* studies in experimental therapeutics focus on the effect of treatments on isolated tumors and few make use of metastatic animal models [34]. However, we and others have previously shown that differential effects occur on the primary tumor and the metastases for some anti-cancer drugs, such as the multitargeted tyrosine kinase inhibitor sunitinib [10,11,35]. Similarly, apart from efforts focusing on evolutionary dynamics of metastasis that do not make use of longitudinal data on size kinetics [36], few quantitative mathematical models exist for metastatic development [4,23,37,38], and none has been quantitatively validated for systemic therapy beyond theoretical considerations [37,39,40]. In previous work we first established such a mathematical model featuring natural metastatic development and surgery of the primary tumor, but no systemic treatment [4]. This was a critical step before being able to model the effect of systemic treatments such as NAT where treatments are limited and long-term benefits are presumed but difficult to quantify because disease recurrence can happen years after surgery, or not recur at all. In the current study, we extended our mathematical model to examine NAT with the RTKI sunitinib by using longitudinal data from 128 mice (more than four times more than previous studies [4,38]). Such a large number of subjects and tightly controlled experimental conditions (genetically identical animal background, cell origin, treatment periods, etc..), resulted in precise estimates of the model parameters.

We and others have demonstrated that robust inhibition of primary tumor growth does not always translate into inhibition of metastasis post-surgically nor improvement in survival [10,11,41]. This represents a challenge observed clinically with RTKIs: despite decades of potent tumor-reducing effects in mouse models, efficacy in patients with metastatic disease could be underwhelming. Our mechanistic mathematical modeling approach offered a quantitative tool to simulate and test distinct biological scenarios, in order to distinguish the biological determinants underlying this paradoxical differential effect on the primary and distant tumors. Model predictions (with no fitting involved) allowed to disentangle the impact on MB of either PT growth arrest alone or PT and metastases growth arrest. They clearly showed: 1) that metastases growth arrest during NAT was very unlikely and 2) that the quantitative impact of PT growth suppression during NAT was sufficient to reproduce the experimental data. Furthermore, it implied a negligible reduction in dissemination, as measured by the total MB.

These findings could be explained by the fact that the primary tumor (in the mammary fat pad) and the secondary tumors (mostly in the lungs) would rely on different growth mechanisms, especially at small sizes. Supporting this explanation, a study showed that metastasis relied more on vessel co-option rather than angiogenesis, thus providing them a mechanism of resistance to VEGF RTKI therapy [42]. Beyond NAT, our model predicts limited efficacy of sunitinib in the postsurgical setting, because metastases would likely be similarly small and rely on similar growth mechanisms. Interestingly, experimental results in mice confirmed this prediction where using a similar metastatic experimental system of triple-negative breast cancer, adjuvant sunitinib did not improve survival [43].

The mechanistic model of NAT validated here provides a valuable tool to explore the impact of the treatment schedules on response and relapse. Simulating varying durations and doses of NAT, we found that long durations of NAT could significantly increase the risk of metastatic relapse when PT response was moderate. Further, our model provides the computational basis to analyze the impact of various NAT dosing regimens in terms of sequence, breaks, and frequency, which is the topic of a companion work.

For breast cancer patients diagnosed with localized disease, predicting the risk and timing of distant metastatic relapse is a major clinical concern [44–46]. Accurate ways to predict the extent of invisible metastatic disease at diagnosis and risk of future metastatic relapse could help to personalize perioperative therapy protocols and avoid highly toxic therapies to patients with low risk of relapse [45]. However, only two risk models [47,48] have met the AJCC criteria for prognostic tool quality so far [49], and both rely on classical Cox regression survival models. Recently, we have developed a mechanistic approach to metastatic relapse prediction [50]. However, this work did not include the impact of NAT or any systemic treatment. The mathematical model that we validated here on animal data, combined with the methodology developed in [50] lays the groundwork for applications in the clinical NAT setting. It could further refine individual predictions of metastatic relapse in breast cancer by providing surrogate markers of long-term outcomes in addition to pathologic complete response [51]. Indeed, the NAT period represents an invaluable window of opportunity to gather both longitudinal data (such as kinetics of tumor size or pharmacodynamic marker, or circulating DNA from liquid biopsies) and one-time biomarkers from tumor tissue [2]. Here, we propose that mathematical models could form the basis of digital tools able to integrate this multi-parametric and dynamic data into predictive algorithms of both long-term outcome and disease sensitivity to systemic therapy in case of distant relapse.

In the era of artificial intelligence [52], it is to be expected that an increasing number of such prognosis models will appear, combining advances in cancer biology (e.g. molecular gene signatures [45,53]) and imaging [54,55] with algorithmic engineering. Recent years have witnessed the generalization of methods going beyond classical statistical analysis, grouped by the generic term of machine learning (ML) [56]. Here, we proposed an approach to combine ML with mechanistic modeling that consists of using biomarkers at surgery to predict individual mathematical parameters and subsequently postsurgical metastatic evolution. We found overall that the investigated biomarkers contained only limited predictive power of μ, suggesting that alternative biomarkers should be explored in future preclinical and clinical studies. This contrasts with reports showing Ki67 as significantly associated with the risk of metastatic relapse [57]. It might be because Ki67 is a proliferation marker [58], which should rather be predictive of α or the doubling time. Such correlation was observed between Ki67+/CD31+ and DT (Fig 3E), as well as clinical work using our modeling approach [50]. Paired with early clinical trials, our *in vivo/in silico* approach could have translational value to improve biomarkers screening.

Important limitations of our study are that we only analyzed data from one tumor type (triple negative breast cancer), one cell line in one, immune-depressed, animal system, and one drug. This might alter the generalizability and possibly translation of preclinical findings to clinical situations. On the other hand, this is a necessary prerequisite to control as much as possible the heterogeneity in the data, which remains substantial

559 despite a tightly controlled experimental setting. Such conditions ensure robust testing
560 of biological assumptions underlying our mathematical models and, eventually,
561 refutation of unplausible ones (here, that primary and secondary growth would be
562 equally suppressed by NAT).

563 Given the increasingly diverse arsenal of systemic anti-cancer therapies available with
564 the approval of immune-checkpoint inhibitors, optimal treatment sequence [12,59–61]
565 and dosing regimen [62,63] are becoming crucial issues. Our model could be used and
566 extended to guide the rational design of treatment schedules and modes of combination
567 of immunotherapy with another systemic drug, before preclinical or clinical testing. For
568 immunotherapy, the model would need to be developed further and at least include an
569 additional systemic variable representing the immune system. Immuno-monitoring
570 quantifications could provide an invaluable source of longitudinal data to feed
571 mechanistic models [64]. In addition, response to neoadjuvant therapy could be used
572 to predict which patients are more likely to benefit from adjuvant therapy [9]. Combining
573 artificial intelligence techniques with mechanistic modeling, our modeling methodology
574 offers a way to perform such predictions quantitatively and possibly personalize
575 therapeutic intervention.

References

1. Escrivá-de-Romaní S, Arumí M, Zamora E, Bellet M. Neoadjuvant Model as a Platform for Research in Breast Cancer and Novel Targets under Development in this Field. Breast Care. 2018;13(4):251–62.

2. Marron TU, Galsky MD, Taouli B, Fiel MI, Ward S, Kim E, et al. Neoadjuvant clinical trials provide a window of opportunity for cancer drug discovery. Nat Med. 2022 Apr;28(4):626–9.

3. Roarty K, Echeverria GV. Laboratory Models for Investigating Breast Cancer Therapy Resistance and Metastasis. Front Oncol [Internet]. 2021 [cited 2024 Feb 28];11. Available from: https://www.frontiersin.org/journals/oncology/articles/10.3389/fonc.2021.645698

4. Benzekry S, Tracz A, Mastri M, Corbelli R, Barbolosi D, Ebos JM. Modeling spontaneous metastasis following surgery: an in vivo-in silico approach. Cancer Res. 2016 Feb 1;76(3):535–47.

5. Ebos JML, Lee CR, Bogdanovic E, Alami J, Van Slyke P, Francia G, et al. Vascular endothelial growth factor-mediated decrease in plasma soluble vascular endothelial growth factor receptor-2 levels as a surrogate biomarker for tumor growth. Cancer Res. 2008 Jan 15;68(2):521–9.

6. Qin S, Li A, Yi M, Yu S, Zhang M, Wu K. Recent advances on anti-angiogenesis receptor tyrosine kinase inhibitors in cancer therapy. J Hematol OncolJ Hematol Oncol. 2019 Mar 12;12:27.

7. Aalders KC, Tryfonidis K, Senkus E, Cardoso F. Anti-angiogenic treatment in breast cancer: Facts, successes, failures and future perspectives. Cancer Treat Rev. 2017 Feb 1;53:98–110.

8. von Minckwitz G, Eidtmann H, Rezai M, Fasching PA, Tesch H, Eggemann H, et al. Neoadjuvant chemotherapy and bevacizumab for HER2-negative breast cancer. N Engl J Med. 2012 Jan 26;366(4):299–309.

9. Bear HD, Tang G, Rastogi P, Geyer CE, Robidoux A, Atkins JN, et al. Bevacizumab added to neoadjuvant chemotherapy for breast cancer. N Engl J Med. 2012 Jan 26;366(4):310–20.

10. Ebos JML, Mastri M, Lee CR, Tracz A, Hudson JM, Attwood K, et al. Neoadjuvant antiangiogenic therapy reveals contrasts in primary and metastatic tumor efficacy. EMBO Mol Med. 2014 Dec;6(12):1561–76.

11. Ebos JML, Lee CR, Cruz-Munoz W, Bjarnason GA, Christensen JG, Kerbel RS. Accelerated metastasis after short-term treatment with a potent inhibitor of tumor angiogenesis. Cancer Cell. 2009 Mar 3;15(3):232–9.

12. Ciccolini J, Barbolosi D, André N, Barlesi F, Benzekry S. Mechanistic Learning for Combinatorial Strategies With Immuno-oncology Drugs: Can Model-Informed Designs Help Investigators? JCO Precis Oncol. 2020 May 1;(4):486–91.

13. Benzekry S. Artificial intelligence and mechanistic modeling for clinical decision making in oncology. Clin Pharmacol Ther. 2020;108(3):471–86.

14. Rajkomar A, Dean J, Kohane I. Machine Learning in Medicine. N Engl J Med. 2019 Apr 4;380(14):1347–58.

15. Breiman L. Statistical modeling: the two cultures. Stat Sci Rev J Inst Math Stat. 2001 Jan 1;16(3):199–231.

16. Mastri M, Benzekry S, Ebos JM. Pre- and post-surgical monitoring of experimental primary tumor growth and metastasis under neo-adjuvant treatment [Internet]. Zenodo; 2024 [cited 2024 Feb 28]. Available from: https://zenodo.org/records/10607753

17. Benzekry S. metamats.burden.treatment – Software Heritage archive [Internet]. [cited 2024 Apr 7]. Available from: https://archive.softwareheritage.org/swh:1:snp:d39660e34a46938dba993b474433a38b7c51a70f;origin=https://gitlab.inria.fr/benzekry/metamats.burden.treatment

18. Faivre S, Demetri G, Sargent W, Raymond E. Molecular basis for sunitinib efficacy and future clinical development. Nat Rev Drug Discov. 2007 Sep;6(9):734–45.

19. Mastri M, Tracz A, Lee CR, Dolan M, Attwood K, Christensen JG, et al. A Transient Pseudosenescent Secretome Promotes Tumor Growth after Antiangiogenic Therapy Withdrawal. Cell Rep. 2018 Dec 26;25(13):3706-3720.e8.

20. Suresh K. An overview of randomization techniques: An unbiased assessment of outcome in clinical research. J Hum Reprod Sci. 2011 Jan;4(1):8–11.

21. Wheldon TE. Mathematical Models in Cancer Research,. 1 edition. Bristol: CRC Press; 1988. 264 p.

22. Spratt JS, Meyer JS, Spratt JA. Rates of growth of human solid neoplasms: Part I. J Surg Oncol. 1995 Oct 1;60(2):137–46.

23. Iwata K, Kawasaki K, Shigesada N. A dynamical model for the growth and size distribution of multiple metastatic tumors. J Theor Biol. 2000 Mar 21;203(2):177–86.

24. Hartung N. Efficient resolution of metastatic tumor growth models by reformulation into integral equations. Discrete Contin Dyn Syst Ser B. 2015 Mar 1;20(2):445–67.

25. Norton L, Simon R. Tumor size, sensitivity to therapy, and design of treatment schedules. Cancer Treat Rep. 1977 Jan 1;61:1307–17.

26. Zhou Q, Gallo JM. Quantification of sunitinib in mouse plasma, brain tumor and normal brain using liquid chromatography-electrospray ionization-tandem mass spectrometry and pharmacokinetic application. J Pharm Biomed Anal. 2010 Mar 11;51(4):958.

27. Lavielle M. Mixed Effects Models for the Population Approach: Models, Tasks, Methods and Tools. 2014.

28. Matlab with statistics and optimization toolboxes. The Mathworks Inc.; 2015.

29. Pollard JW. Defining Metastatic Cell Latency. N Engl J Med. 2016 juillet;375(3):280–2.

30. Max Kuhn. Contributions from Jed Wing, Steve Weston, Andre Williams, Chris Keefer, Allan Engelhardt, Tony Cooper, Zachary Mayer, Brenton Kenkel, the R Core Team, Michael Benesty, Reynald Lescarbeau, Andrew Ziem, Luca Scrucca, Yuan Tang, Can Candan and Tyler Hunt. (2018). caret: Classification and Regression Training. R package version 6.0-80. https://CRAN.R-project.org/package=caret.

31. R Core Team (2018). R: A language and environment for statistical computing. R Foundation for Statistical Computing, Vienna, Austria. URL https://www.R-project.org/.

32. Savic RM, Karlsson MO. Importance of Shrinkage in Empirical Bayes Estimates for Diagnostics: Problems and Solutions. AAPS J. 2009 Aug 1;11(3):558–69.

33. Kuhn M, Johnson K. Applied predictive modeling. Vol. 26. Springer; 2013.

34. Francia G, Cruz-Munoz W, Man S, Xu P, Kerbel RS. Mouse models of advanced spontaneous metastasis for experimental therapeutics. Nat Rev Cancer. 2011 Feb 1;11(2):135–41.

35. Paez-Ribes M, Allen E, Hudock J, Takeda T, Okuyama H, ViNals F, et al. Antiangiogenic therapy elicits malignant progression of tumors to increased local invasion and distant metastasis. 2009 Mar 1;15(3):220–31.

36. Reiter JG, Makohon-Moore AP, Gerold JM, Heyde A, Attiyeh MA, Kohutek ZA, et al. Minimal functional driver gene heterogeneity among untreated metastases. Science. 2018 Sep 7;361(6406):1033–7.

37. Haeno H, Gonen M, Davis MB, Herman JM, Iacobuzio-Donahue CA, Michor F. Computational Modeling of Pancreatic Cancer Reveals Kinetics of Metastasis Suggesting Optimum Treatment Strategies. Cell. 2012;148(1):362–75.

38. Hartung N, Mollard S, Barbolosi D, Benabdallah A, Chapuisat G, Henry G, et al. Mathematical modeling of tumor growth and metastatic spreading: validation in tumor-bearing mice. Cancer Res. 2014 Nov 15;74(22):6397–407.

39. Benzekry S, André N, Benabdallah A, Ciccolini J, Faivre C, Hubert F, et al. Modelling the impact of anticancer agents on metastatic spreading. Math Model Nat Phenom. 2012 Jan 1;7(1):306–36.

40. Benzekry S, Hahnfeldt P. Maximum tolerated dose versus metronomic scheduling in the treatment of metastatic cancers. J Theor Biol. 2013 Oct 1;335:235–44.

41. Ebos JML. Prodding the Beast: Assessing the Impact of Treatment-Induced Metastasis. Cancer Res. 2015 Sep 1;75(17):3427–35.

42. Bridgeman VL, Vermeulen PB, Foo S, Bilecz A, Daley F, Kostaras E, et al. Vessel co-option is common in human lung metastases and mediates resistance to anti-angiogenic therapy in preclinical lung metastasis models. J Pathol. 2017 Feb;241(3):362–74.

43. Wu FTH, Xu P, Chow A, Man S, Krüger J, Khan KA, et al. Pre- and post-operative anti-PD-L1 plus anti-angiogenic therapies in mouse breast or renal cancer models of micro- or macro-metastatic disease. Br J Cancer. 2019 Jan;120(2):196–206.

44. Krop I, Ismaila N, Andre F, Bast RC, Barlow W, Collyar DE, et al. Use of Biomarkers to Guide Decisions on Adjuvant Systemic Therapy for Women With Early-Stage Invasive Breast Cancer: American Society of Clinical Oncology Clinical Practice Guideline Focused Update. J Clin Oncol. 2017 Jul 10;35(24):2838–47.

45. Cardoso F, van't Veer LJ, Bogaerts J, Slaets L, Viale G, Delaloge S, et al. 70-Gene Signature as an Aid to Treatment Decisions in Early-Stage Breast Cancer. N Engl J Med. 2016 Aug 25;375(8):717–29.

46. Senkus E, Kyriakides S, Ohno S, Penault-Llorca F, Poortmans P, Rutgers E, et al. Primary breast cancer: ESMO Clinical Practice Guidelines for diagnosis, treatment and follow-up. Ann Oncol. 2015 Sep 1;26 Suppl 5(suppl 5):v8–30.

47. Ravdin PM, Siminoff LA, Davis GJ, Mercer MB, Hewlett J, Gerson N, et al. Computer program to assist in making decisions about adjuvant therapy for women with early breast cancer. J Clin Oncol. 2001 février;19(4):980–91.

48. Wishart GC, Azzato EM, Greenberg DC, Rashbass J, Kearins O, Lawrence G, et al. PREDICT: a new UK prognostic model that predicts survival following surgery for invasive breast cancer. Breast Cancer Res. 2010 Jan 1;12(1):R1.

49. Hortobagyi GN, Connolly JL, DOrsi CJ, Edge S, Mittendorf E, Rugo HS, et al. AJCC Cancer Staging Manual - Breast Cancer. In: Amin MB, Edge S, Greene F, Byrd DR, Brookland RK, Washington MK, et al., editors. AJCC Cancer Staging Manual. Springer International Publishing; 2017.

50. Nicolò C, Périer C, Prague M, Bellera C, MacGrogan G, Saut O, et al. Machine Learning and Mechanistic Modeling for Prediction of Metastatic Relapse in Early-Stage Breast Cancer. JCO Clin Cancer Inform. 2020 Mar 26;4:259–74.

51. Conforti F, Pala L, Bagnardi V, De Pas T, Colleoni M, Buyse M, et al. Surrogacy of Pathologic Complete Response in Trials of Neoadjuvant Therapy for Early Breast Cancer: Critical Analysis of Strengths, Weaknesses, and Misinterpretations. JAMA Oncol. 2022 Nov 1;8(11):1668–75.

52. Topol EJ. High-performance medicine: the convergence of human and artificial intelligence. Nat Med. 2019 Jan 1;25(1):44–56.

53. Perou CM, Sørlie T, Eisen MB, van de Rijn M, Jeffrey SS, Rees CA, et al. Molecular portraits of human breast tumours. Nature. 2000 août;406(6797):747–52.

54. Limkin EJ, Sun R, Dercle L, Zacharaki EI, Robert C, Reuzé S, et al. Promises and challenges for the implementation of computational medical imaging (radiomics) in oncology. Ann Oncol. 2017 juin;28(6):1191–206.

55. Kather JN, Krisam J, Charoentong P, Luedde T, Herpel E, Weis CA, et al. Predicting survival from colorectal cancer histology slides using deep learning: A retrospective multicenter study. Butte AJ, editor. PLOS Med. 2019 Jan 1;16(1):e1002730.

56. Kourou K, Exarchos TP, Exarchos KP, Karamouzis MV, Fotiadis DI. Machine learning applications in cancer prognosis and prediction. Comput Struct Biotechnol J. 2015;13:8–17.

57. Yerushalmi R, Woods R, Ravdin PM, Hayes MM, Gelmon KA. Ki67 in breast cancer: prognostic and predictive potential. Lancet Oncol. 2010 Feb 1;11(2):174–83.

58. Dowsett M, Nielsen TO, A'Hern R, Bartlett J, Coombes RC, Cuzick J, et al. Assessment of Ki67 in breast cancer: recommendations from the International Ki67 in Breast Cancer working group. J Natl Cancer Inst. 2011 Nov 16;103(22):1656–64.

59. Imbs DC, El Cheikh R, Boyer A, Ciccolini J, Mascaux C, Lacarelle B, et al. Revisiting Bevacizumab + Cytotoxics Scheduling Using Mathematical Modeling: Proof of Concept Study in Experimental Non-Small Cell Lung Carcinoma. CPT Pharmacomet Syst Pharmacol. 2018 Jan 1;7(1):42–50.

60. Rothschild S, Zippelius A, Savic S, Gonzalez M, Weder W, Xyrafas A, et al. SAKK 16/14: Anti-PD-L1 antibody durvalumab (MEDI4736) in addition to neoadjuvant chemotherapy in patients with stage IIIA(N2) non-small cell lung cancer (NSCLC)—A multicenter single-arm phase II trial. J Clin Oncol. 2018 May 20;36(15_suppl):TPS8584–TPS8584.

61. Ciccolini J, Barbolosi D, André N, Benzekry S, Barlesi F. Combinatorial immunotherapy strategies: most gods throw dice, but fate plays chess. Ann Oncol. 2019 Nov 1;30(11):1690–1.

62. Reguera-Nuñez E, Man S, Xu P, Kerbel RS. Preclinical impact of high dose intermittent antiangiogenic tyrosine kinase inhibitor pazopanib in intrinsically resistant tumor models. Angiogenesis. 2018 Nov;21(4):793–804.

63. Ratain MJ, Goldstein DA. Time Is Money: Optimizing the Scheduling of Nivolumab. J Clin Oncol. 2018 août;JCO.18.00045-4.

64. Ciccolini J, Benzekry S, Barlesi F. Deciphering the response and resistance to immune-checkpoint inhibitors in lung cancer with artificial intelligence-based analysis: when PIONeeR meets QUANTIC. Br J Cancer. 2020 Jun 16;1–2.

Supplementary information legends

S1 Table: Neoadjuvant treatment schedules and doses

Animal groups showing treatment schedules and dosing during a presurgical neoadjuvant period of 14 days.

S1 Fig. Comparison of simulation of therapy (A) vs no therapy (B) on metastases

S2 Fig. Population fits of all the groups used to calibrate the model parameters (surgery at day 34)

S3 Fig. Representative individual fits of the model for Sunitinib-treated animals

S4 Fig. Model predictions in independent datasets (surgery at day 38)

S5 Fig. Model diagnostic plots

(A) Observation vs. individual prediction. Solid lines are identity lines. Dashed lines represent 90% prediction intervals.

(B) Individual weighted residuals (IWRES) vs time.

(C) Individual weighted residuals vs log-transformed individual predictions.

S6 Fig. Distribution of the individual parameters

S7 Fig. Correlations between random effects

S8 Fig. Individual parameters vs covariates

S9 Fig. Observed vs Predicted values for the machine learning algorithms

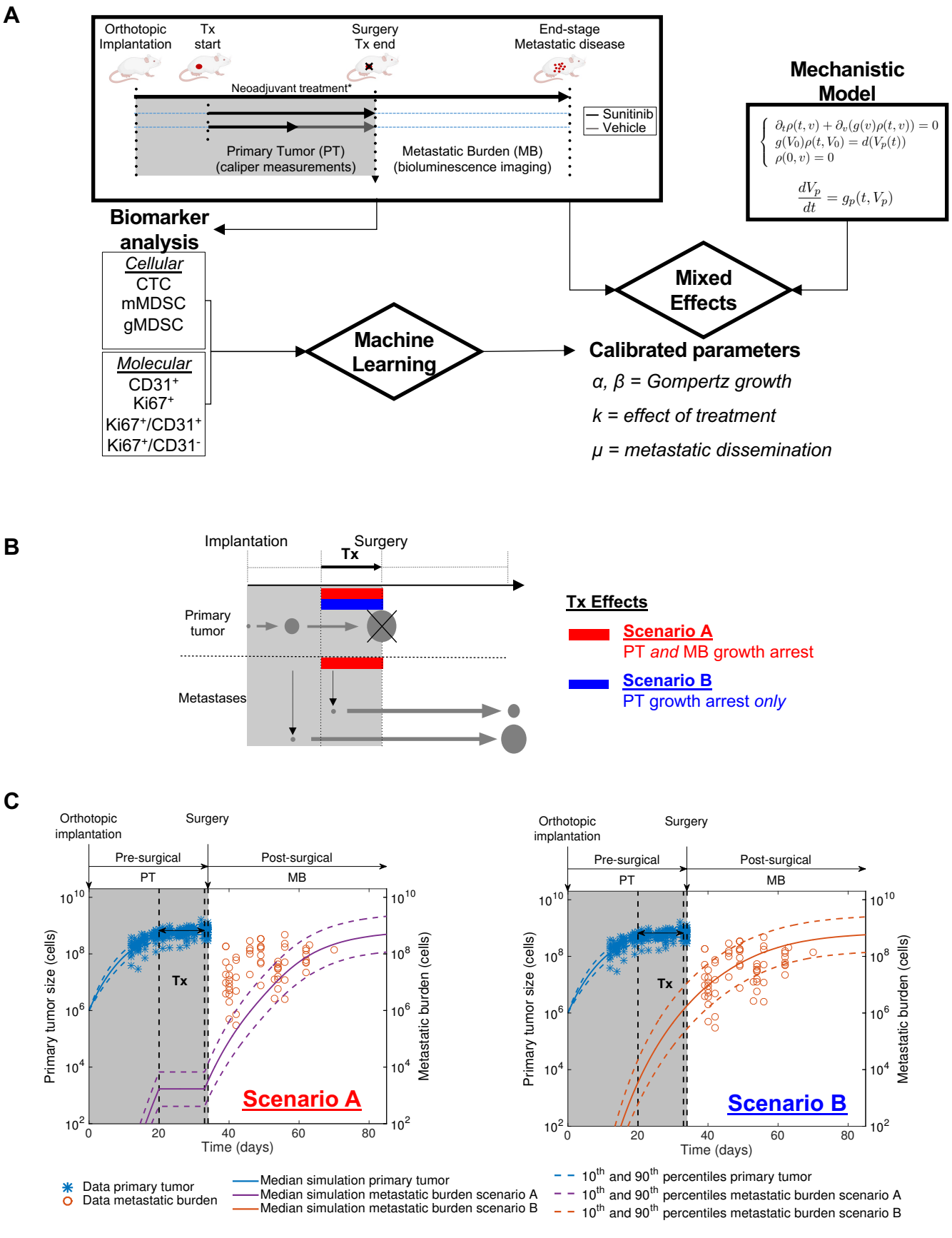
A
Orthotopic Implantation
Tx start
Surgery Tx end
End-stage Metastatic disease
Neoadjuvant treatment*
Sunitinib
Vehicle
Primary Tumor (PT) (caliper measurements)
Metastatic Burden (MB) (bioluminescence imaging)
Mechanistic Model
$\begin{cases} \partial_t \rho(t,v) + \partial_v(g(v)\rho(t,v)) = 0 \\ g(V_0)\rho(t,V_0) = d(V_p(t)) \\ \rho(0,v) = 0 \end{cases}$
$\frac{dV_p}{dt} = g_p(t, V_p)$
Biomarker analysis
Cellular
CTC
mMDSC
gMDSC
Molecular
CD31+
Ki67+
Ki67+/CD31+
Ki67+/CD31-
Machine Learning
Mixed Effects
Calibrated parameters
α, β = Gompertz growth
k = effect of treatment
μ = metastatic dissemination
B
Implantation
Surgery
Tx
Primary tumor
Metastases
Tx Effects
Scenario A
PT and MB growth arrest
Scenario B
PT growth arrest only
C
Orthotopic implantation
Surgery
Pre-surgical
Post-surgical
PT
MB
Tx
Primary tumor size (cells)
Metastatic burden (cells)
Time (days)
Scenario A
Scenario B
Data primary tumor
Data metastatic burden
Median simulation primary tumor
Median simulation metastatic burden scenario A
Median simulation metastatic burden scenario B
10th and 90th percentiles primary tumor
10th and 90th percentiles metastatic burden scenario A
10th and 90th percentiles metastatic burden scenario B

Figure 1: Mathematical modeling reveals differential effects of neoadjuvant sunitinib treatment on primary tumor and metastatic growth.

(A) Schematic of the study. Data from an ortho-surgical, human xenograft animal model of neoadjuvant sunitinib breast cancer treatment were fitted using a mixed-effects statistical framework. This provided calibrated parameters for each animal. Machine learning algorithms were used to assess the predictive power of molecular and cellular biomarkers to predict the metastatic dissemination parameter μ and quantify metastatic aggressiveness.
(B) Schematic of tested hypotheses of the effect of neoadjuvant sunitinib Tx on primary tumor and metastatic growth and dissemination through mechanistic mathematical modeling. Scenario A = growth arrest on both primary and secondary tumors. Scenario B = growth arrest on primary tumor only.
(C) Predicted simulations of Scenarios A and B using parameters calibrated from a previous study [Benzekry et al., Cancer Res, 2016] involving untreated (vehicle) animals only. Data plotted here (LM2-4^{LUC+} bioluminescent human breast cancer cells orthotopically injected in mice) was not used to estimate the model parameters.

*Tx, treatment; PT, primary tumor; MB, metastatic burden. *See methods for additional details on animal experiments, treatment dose and duration, and mechanistic model.*

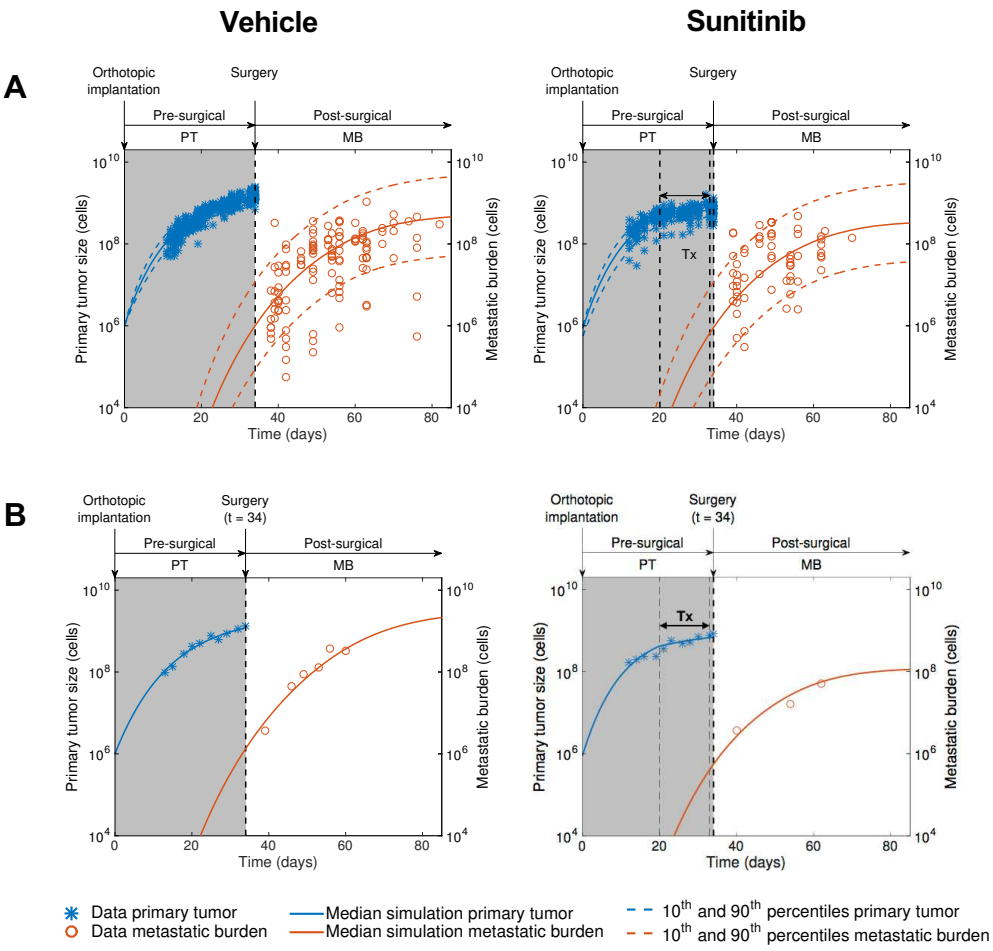
Vehicle
Sunitinib
A
B
Orthotopic implantation
Surgery
Surgery (t = 34)
Pre-surgical
Post-surgical
PT
MB
Tx
Primary tumor size (cells)
Metastatic burden (cells)
Time (days)
Data primary tumor
Data metastatic burden
Median simulation primary tumor
Median simulation metastatic burden
10th and 90th percentiles primary tumor
10th and 90th percentiles metastatic burden

Figure 2: Calibration and validation of a kinetics-pharmacodynamics (K-PD) mathematical model for neoadjuvant sunitinib treatment effect on pre- and post-surgical tumor growth

Pre- and postsurgical growth of LM2-4^{LUC+} human metastatic breast carcinomas were measured in multiple groups involving different neoadjuvant treatment modalities (doses and durations). The mathematical model was fitted to the experimental data using a mixed-effects population approach (n = 104 animals in total).
(A) Comparison of the simulated model population distribution (visual predictive check) for vehicle and neoadjuvant sunitinib treatment (60mg/kg/day) 14 days prior to surgery.
(B) Examples of individual dynamics.

Tx, treatment; PT, primary tumor; MB, metastatic burden.

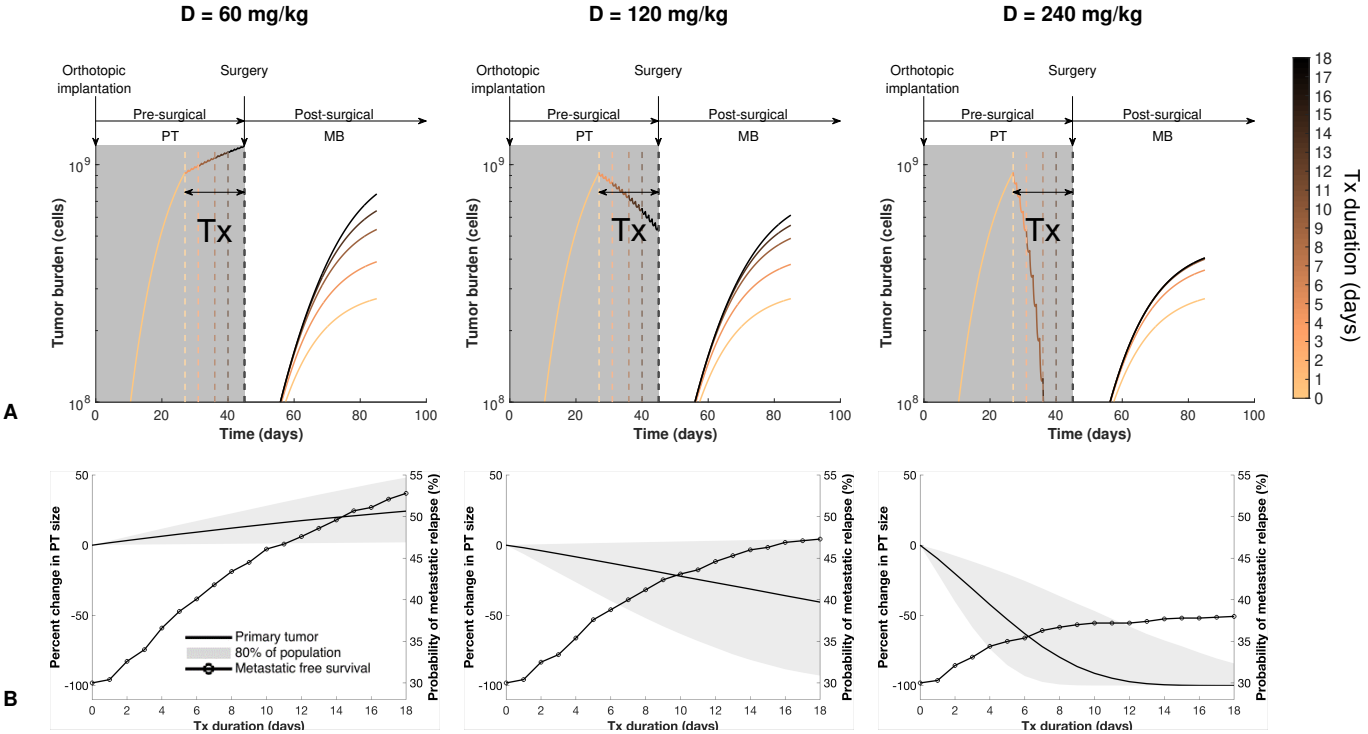
D = 60 mg/kg
D = 120 mg/kg
D = 240 mg/kg
A
B
Orthotopic implantation
Surgery
Pre-surgical
Post-surgical
PT
MB
Tx
Tumor burden (cells)
Time (days)
Tx duration (days)
Percent change in PT size
Probability of metastatic relapse (%)
Tx duration (days)
Primary tumor
80% of population
Metastatic free survival

Figure 3: Simulations of varying neoadjuvant treatment duration quantify contrasted impact on primary tumor size reduction and risk of metastatic relapse

Using model parameters calibrated from data of our ortho-surgical animal model of breast cancer neoadjuvant targeted treatment, simulations were conducted for a treatment durations varying between 0 (light color) and 18 (dark color) days, for three dose levels (60 mg/kg, 120 mg/kg and 240 mg/kg).
(A) Predicted simulations of pre-surgical primary tumor and post-surgical metastatic kinetics. Note: for dose 240 mg/kg, the metastatic burden growth with the three longest treatment durations are superimposed and not distinguishable.
(B) Population-level predictions of final primary tumor size (solid line and grey area) and probability of metastatic relapse as functions of duration of neoadjuvant treatment, which delays surgical removal of primary tumor (circled line). Inter-individual variability simulated from population distribution of the parameters learned from the data (n = 1000 virtual subjects).

Tx, treatment; PT, primary tumor; MB, metastatic burden

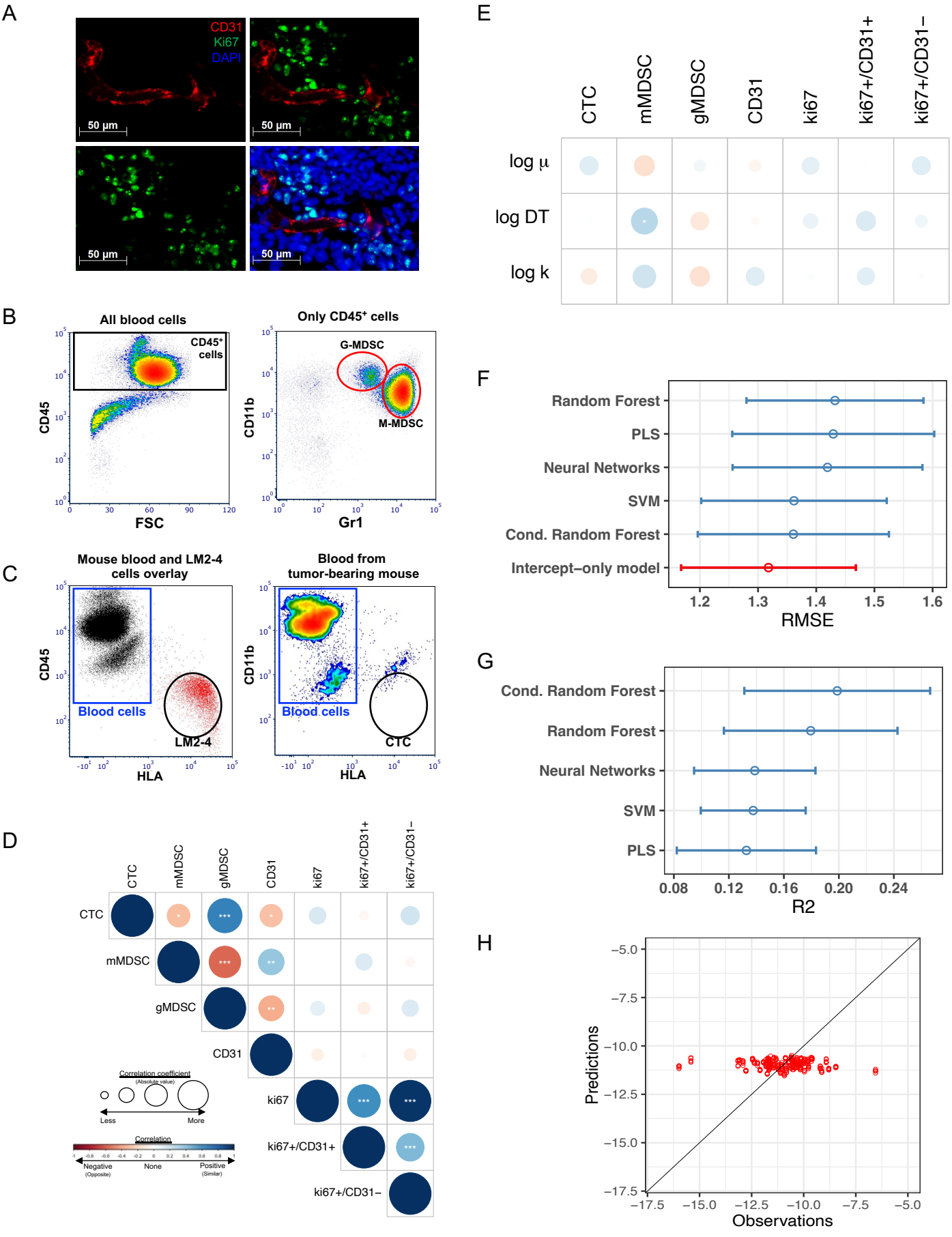
A
CD31
Ki67
DAPI
50 μm
B
All blood cells
CD45⁺ cells
CD45
FSC
Only CD45⁺ cells
G-MDSC
M-MDSC
CD11b
Gr1
C
Mouse blood and LM2-4 cells overlay
Blood cells
LM2-4
CD45
HLA
Blood from tumor-bearing mouse
Blood cells
CTC
CD11b
HLA
D
CTC
mMDSC
gMDSC
CD31
ki67
ki67+/CD31+
ki67+/CD31−
Correlation coefficient
(Absolute value)
Less
More
Correlation
Negative
(Opposite)
None
Positive
(Similar)
E
CTC
mMDSC
gMDSC
CD31
ki67
ki67+/CD31+
ki67+/CD31−
log μ
log DT
log k
F
Random Forest
PLS
Neural Networks
SVM
Cond. Random Forest
Intercept−only model
RMSE
G
Cond. Random Forest
Random Forest
Neural Networks
SVM
PLS
R2
H
Predictions
Observations

Figure 4: Use of machine learning algorithms based on presurgical molecular and cellular markers to predict metastatic dissemination parameter 'μ'.

(A-C) Examples of molecular and cellular biomarker analysis.
(A) Proliferating endothelial cell identification by immunofluorescence. Tissue sections from resected tumors were stained with antibodies against mouse CD31 (red) and mouse Ki67 (green) and counterstained with DAPI (blue). Single channel and merged images are shown. Yellow arrows show proliferating endothelial cells which were counted manually.
(B) Myeloid-Derived Suppressor Cells (MDSC) quantification by flow cytometry. Whole blood was stained with anti-mouse antibodies for CD45, CD11b, and Gr1. After selection of CD45 positive cells MDSCs were analyzed based on CD11b and Gr1 levels. Monocytic-MDSC (M-MDSC) are CD11b+/Gr1high and granulocytic-MDSC (G-MDSC) are CD11b+/Gr1Medium. Examples of MDSC in untreated and treated animals are shown.
(**C)** CTC quantification by flow cytometry. CTCs for xenografts were identified using anti-human HLA. Blood was stained with anti-mouse CD45 and anti-human HLA. Blood and LM2-4 cell samples were overlaid in a dot plot to identify and create the gates for CTCs. Once the gates were created CTC were identified in blood of tumor-bearing mice.
(D) Pearson correlation coefficients between biomarkers. Blue (resp. red) color indicates positive (resp. negative) correlation, with size of the circle proportional to the R^2 correlation coefficient. * *p<0.05, ** p<0.01, *** p<0.001.*
(E) Univariate correlations between the biomarkers and the mathematical parameters. DT = doubling time.
(F) Cross-validated Root Mean Square Error (RMSE) across different machine learning regression models (see methods) utilizing the values of the biomarkers for predicting log(μ). To assess the significance of the covariate in the models, RMSE were compared against the value of this metric obtained using a only-intercept model. Bars are 95% confidence intervals. Shown in red is the model with lowest RMSE. PLS = Partial Least Squares. SVM = Support Vector Machines
(G) Cross validated R2 with 95% confidence intervals.
(H) Predictions versus observations for the conditional random forest algorithm.

Parameter (Unit)	Meaning	Median value	CV (%)	r.s.e. (%)
μ $\left(cell^{-1} \cdot day^{-1}\right)$	Dissemination coefficient	2.12e-11	1.48e+03	17.3
α $\left(day^{-1}\right)$	Gompertzian growth parameter	1.94	18.1	2
β $\left(day^{-1}\right)$	Gompertzian growth parameter	0.0911	19.7	2.21
λ $\left(day^{-1}\right)$	In vitro proliferation rate	0.837 (fixed)	-	-
k (L/mg)	Drug efficacy	0.446	32.1	6.34
k_e $\left(day^{-1}\right)$	Drug elimination rate	3.26 (fixed)	-	-
V_d $\left(day^{-1}\right)$	Drug volume of distribution	12 (fixed)	-	-
$\bar{\sigma}$ (%)	Error parameter	3.91	-	-

Table 1: Parameter estimates of the metastatic and survival models obtained by likelihood maximization via the SAEM algorithm.
Abbreviations: CV, coefficient of variation computed as the ratio of the standard deviation and the median of the estimated parameter distribution; r.s.e., residual standard error.

Table S1:

Group	N	Duration (Days) Sunitinib (mg/kg/day) 120	60	0	Surgery (DPI)	Modeling	Abbrev.
1	6	0	0	14	38	Training	Veh.
2	21	0	0	14	34	Training	Vech.
3	21	0	14	0	34	Training	Su60(14D)
4	6	0	7	7	34	Training	Su60(7D)
5	15	0	3	11	34	Training	Su60(3D)
6	15	3	11	0	34	Training	Su120(3D)/Su60(11D)
7	20	3	0	11	34	Training	Su120(3D)
8	6	3	11	0	38	Validation	Su120(3D)/Su60(11D)
9	6	3	8	3	38	Validation	Su120(3D)/Su60(8D)
10	6	3	4	7	38	Validation	Su120(3D)/Su60(4D)
11	6	3	0	11	38	Validation	Su120(3D)

Table S1: Animal groups showing treatment schedules and dosing during a presurgical neoadjuvant period of 14 days.

Supplementary Figures

Figure S1. Comparison of simulation of therapy (A) vs no therapy (B) on metastases

Surgery at day 34

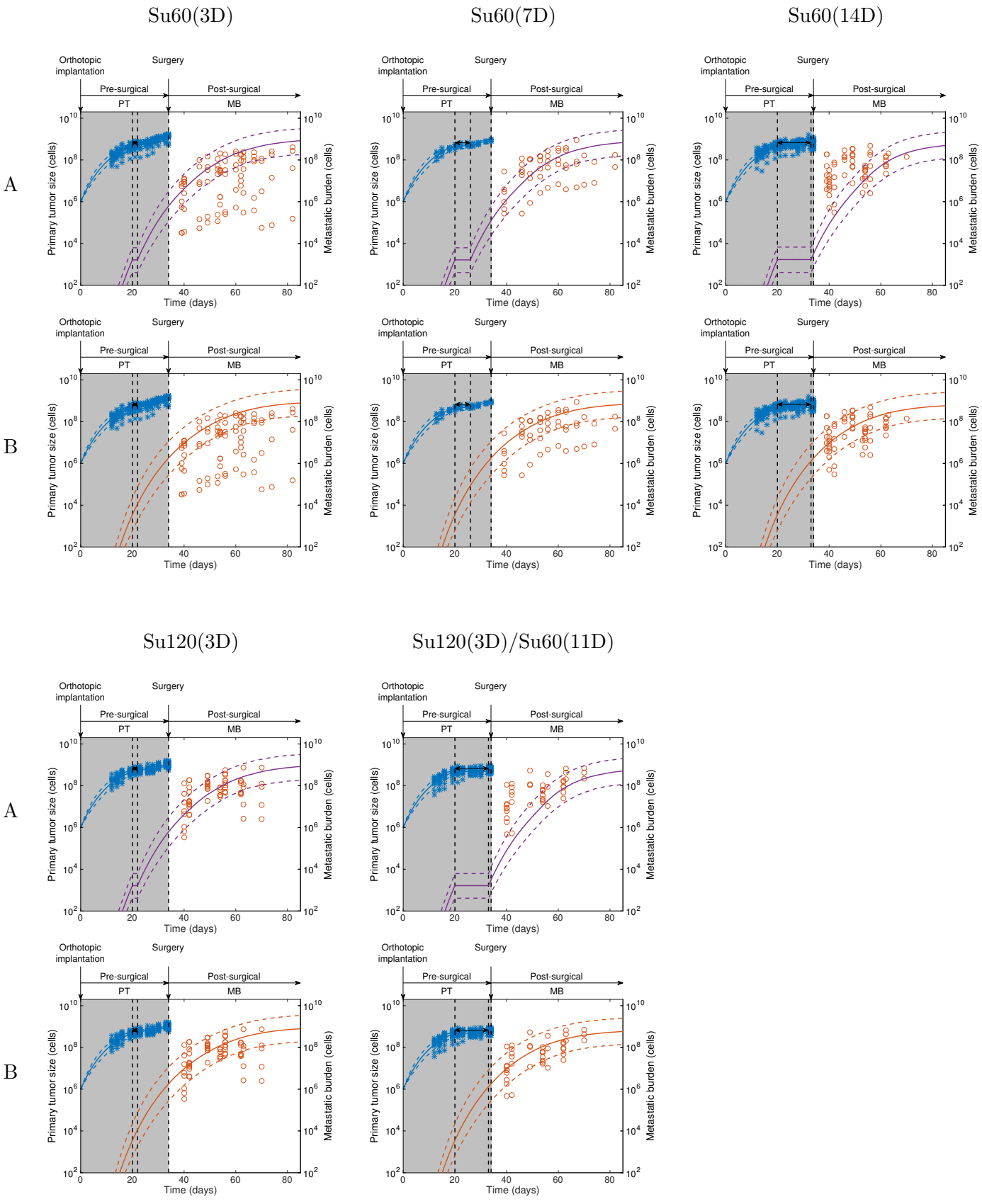

Surgery at day 38

Su120(3D)

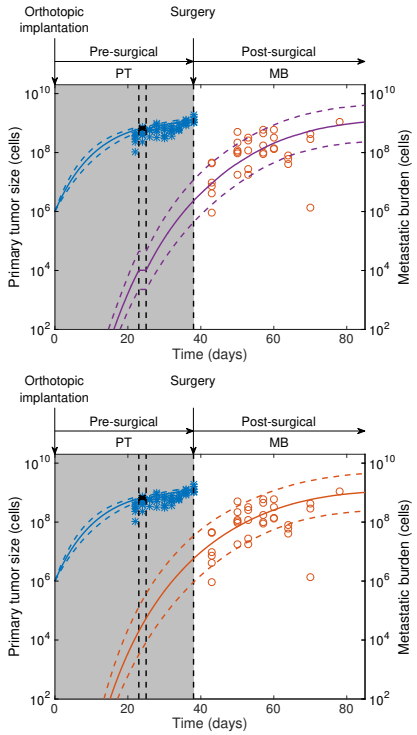

Su120(3D)/Su60(4D)

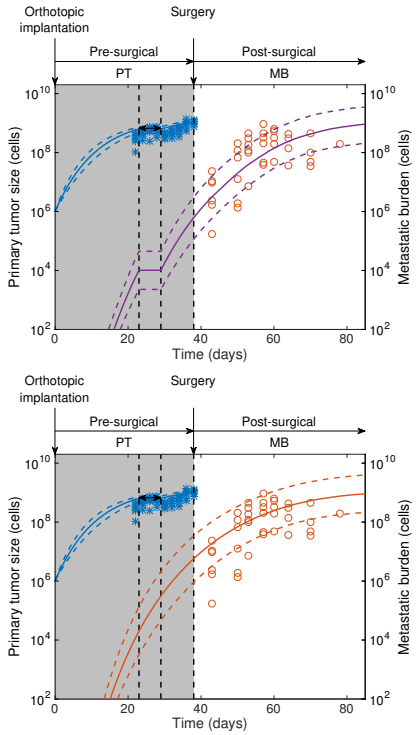

Su120(3D)/Su60(8D)

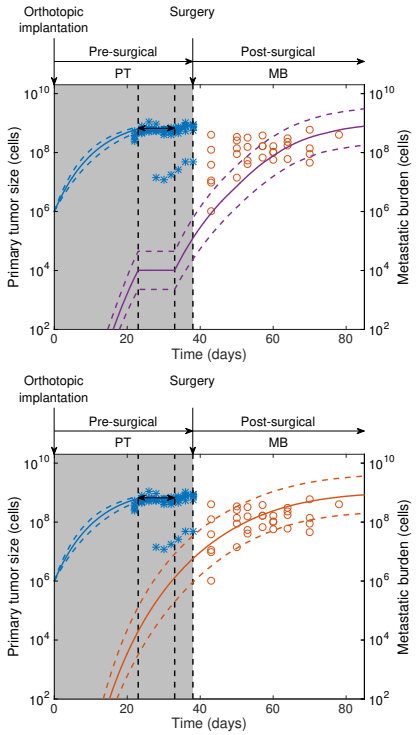

Su120(3D)/Su60(11D)

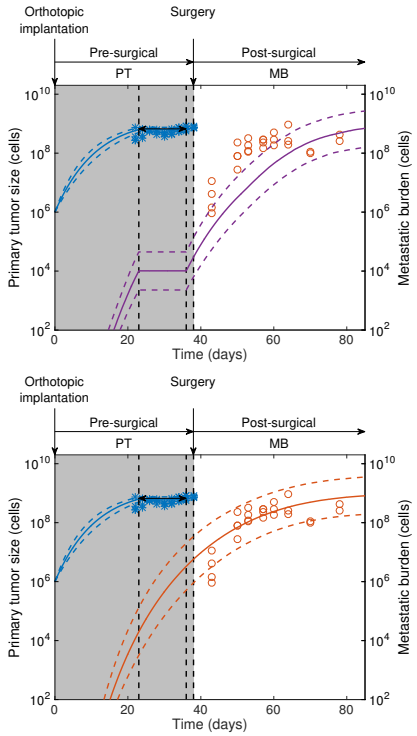

Figure S2. Population fits of all the groups used to calibrate the K-PD model parameters (surgery at day 34)

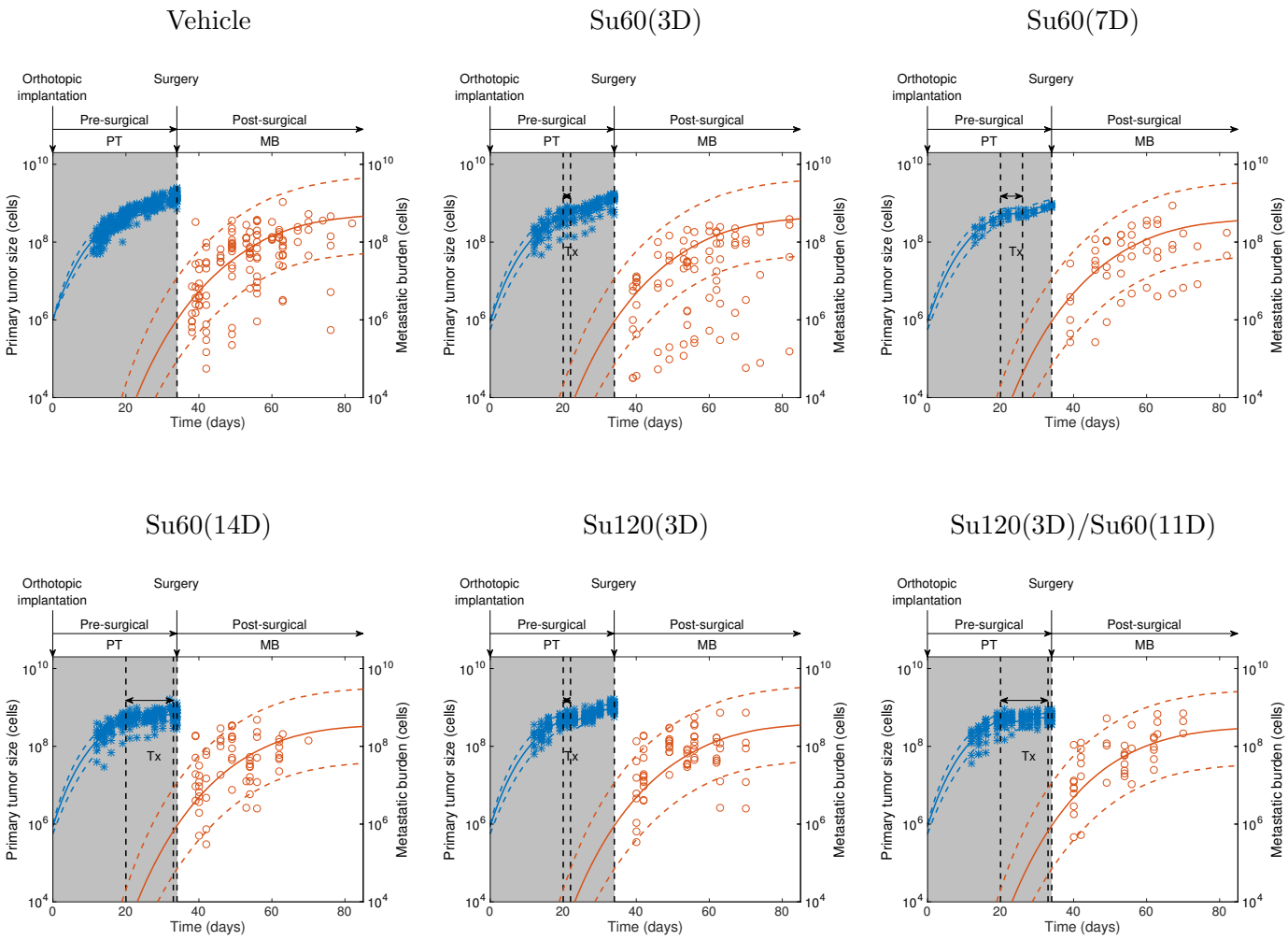

Figure S3. Representative individual fits of the K-PD model for Sunitinib-treated animals

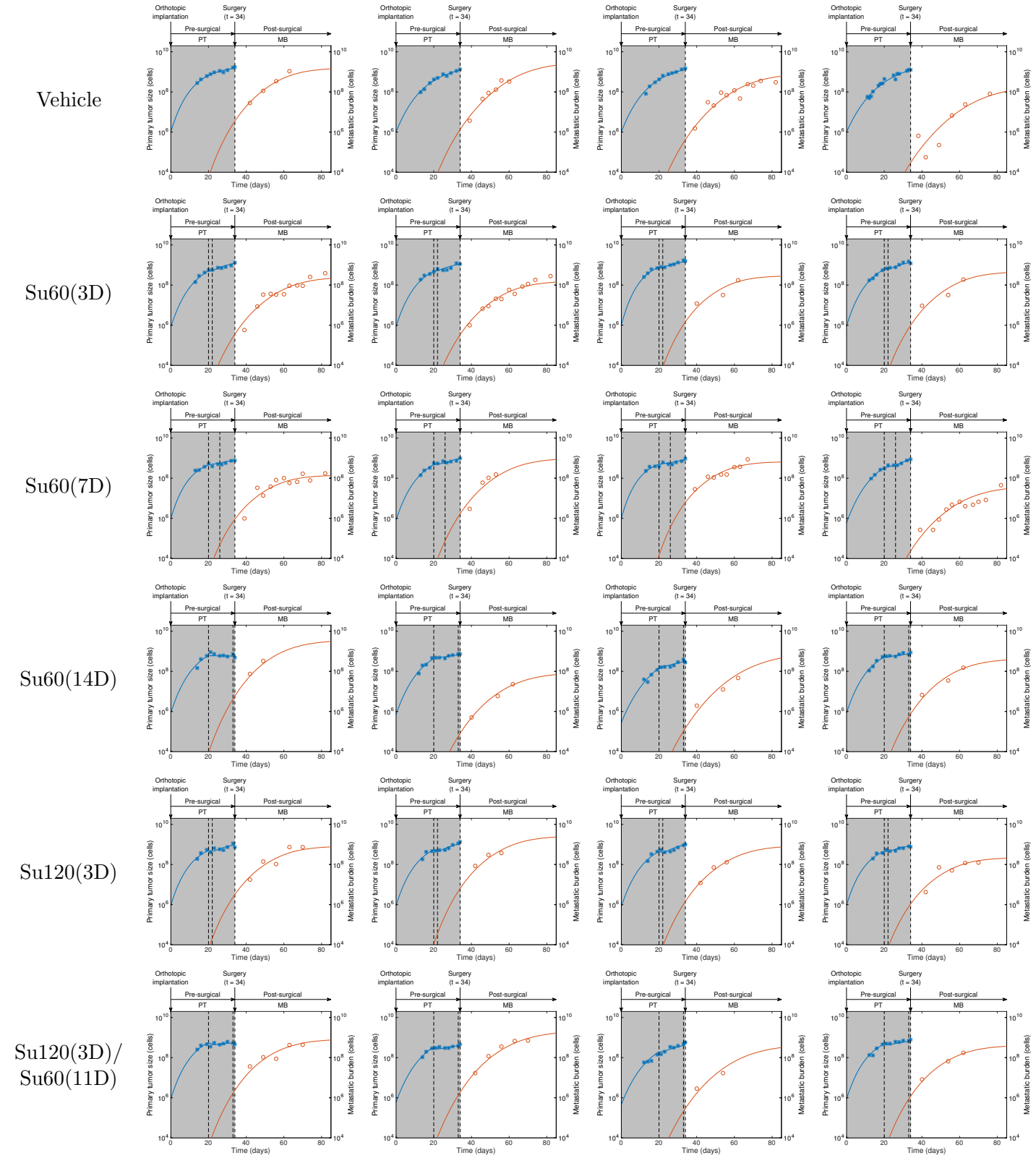

Figure S4. K-PD model predictions in independent datasets (surgery at day 38)

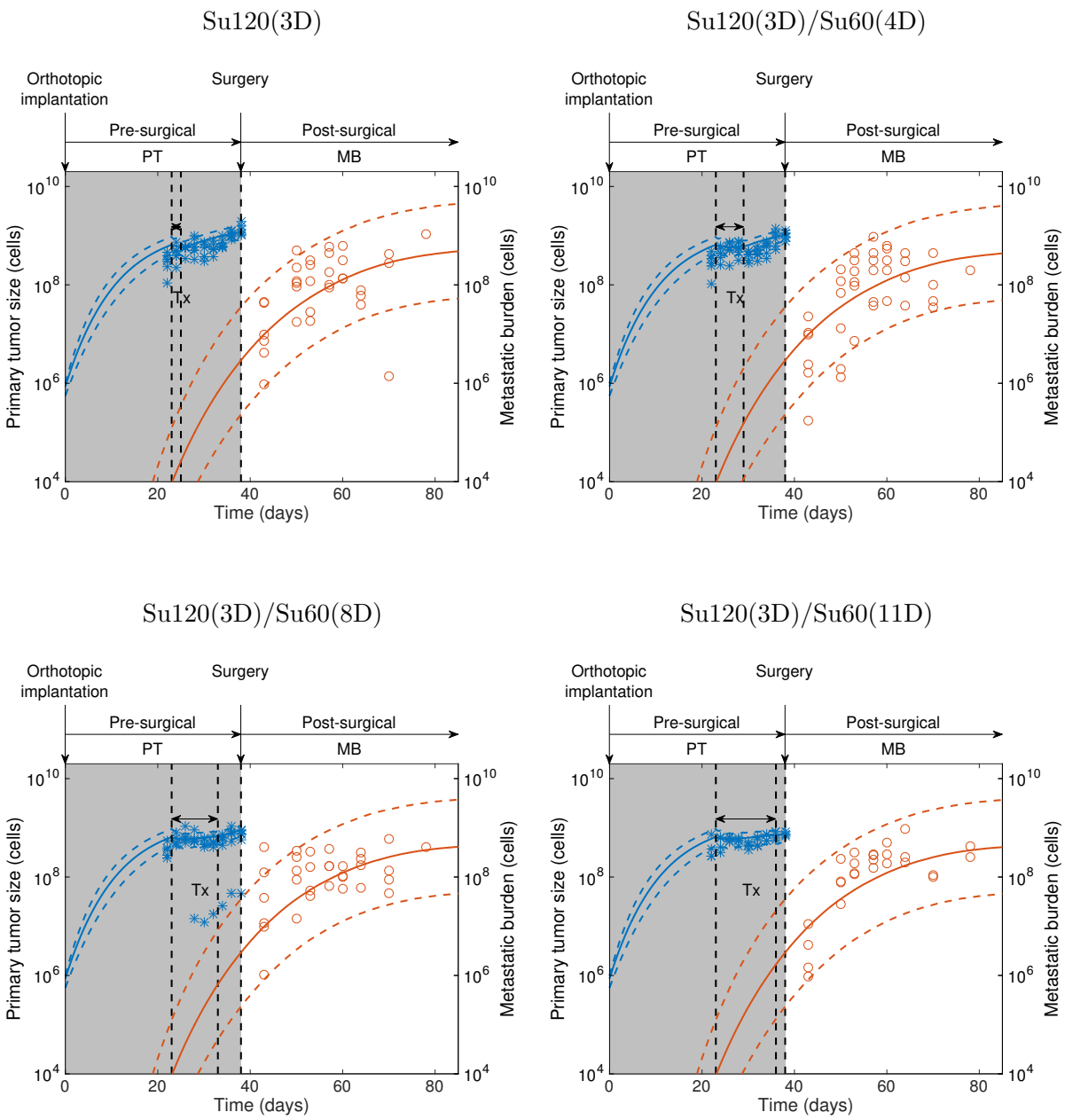

Figure S5. K-PD model diagnostic plots

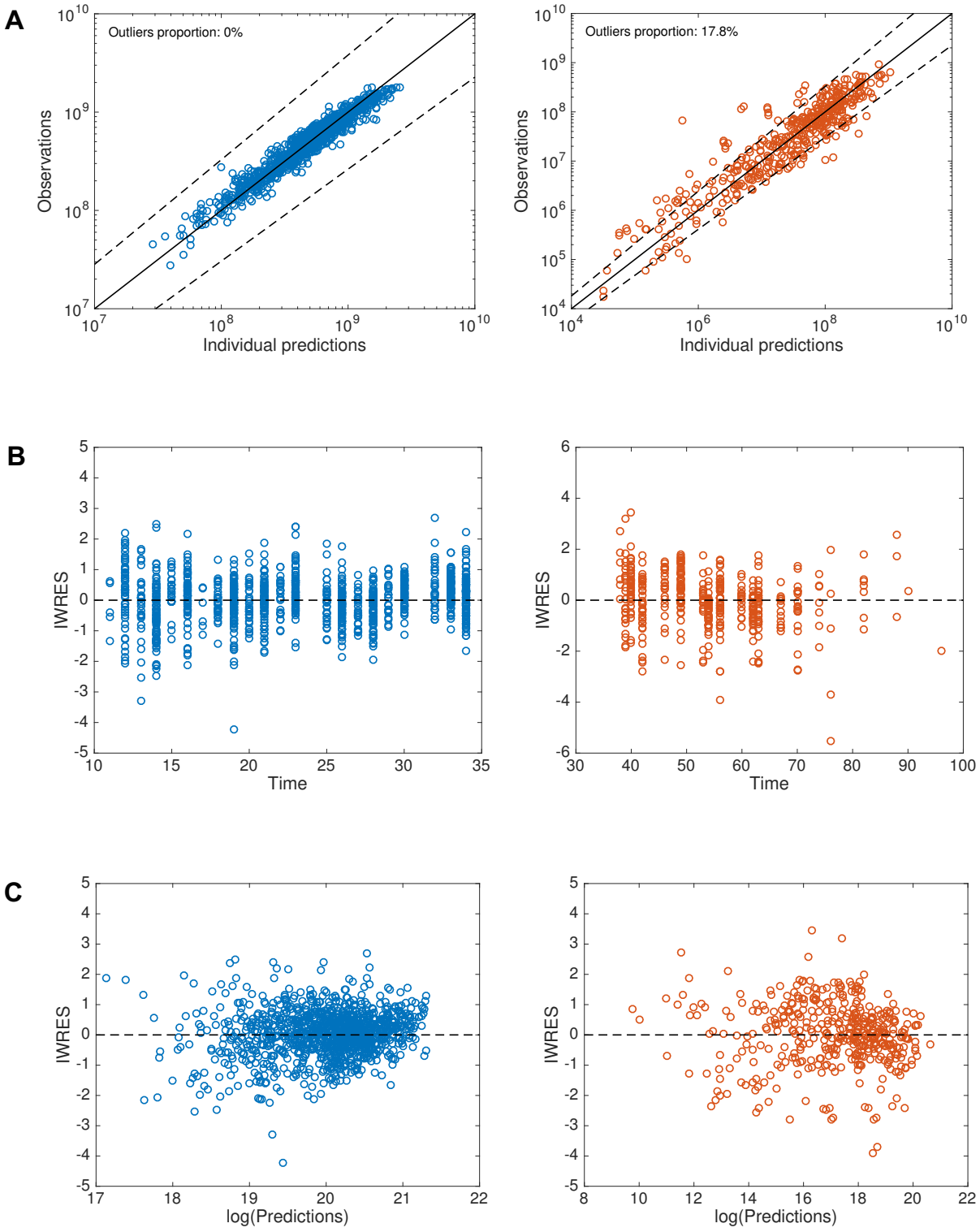

Left (blue): primary tumor, Right (red): metastatic burden.

A) Observation vs. individual prediction. Solid lines are identity lines. Dashed lines represent 90% prediction intervals.

B) Individual weighted residuals (IWRES) vs time.

C) Individual weighted residuals vs log-transformed individual predictions.

Figure S6. Distribution of the individual parameters

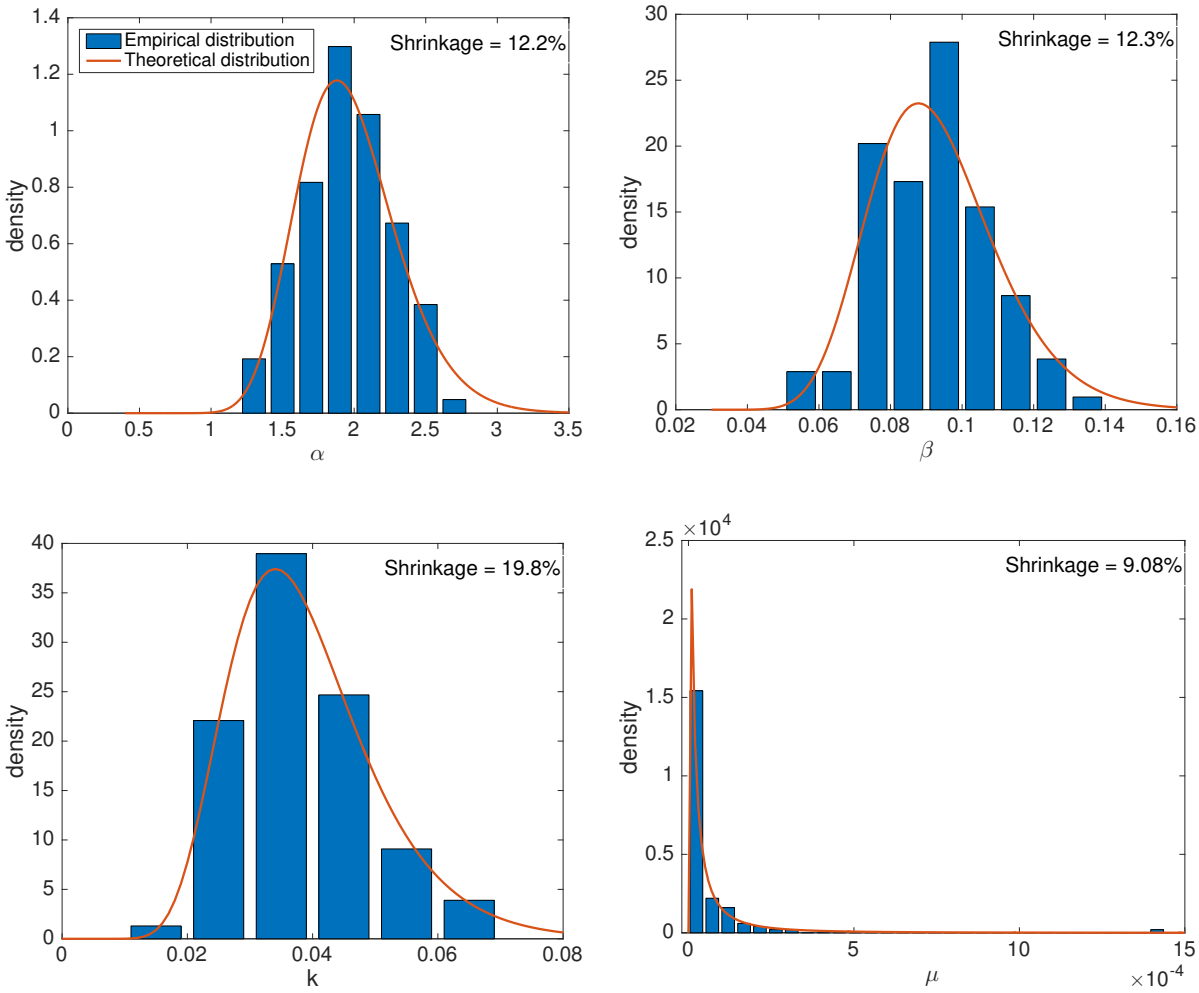

Figure S7. Correlations between random effects

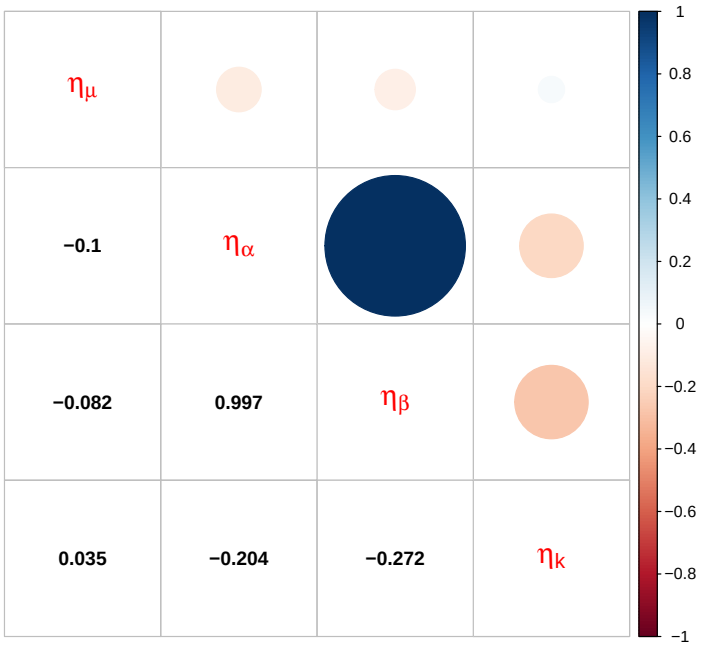

Figure S8. Individual parameters vs covariates

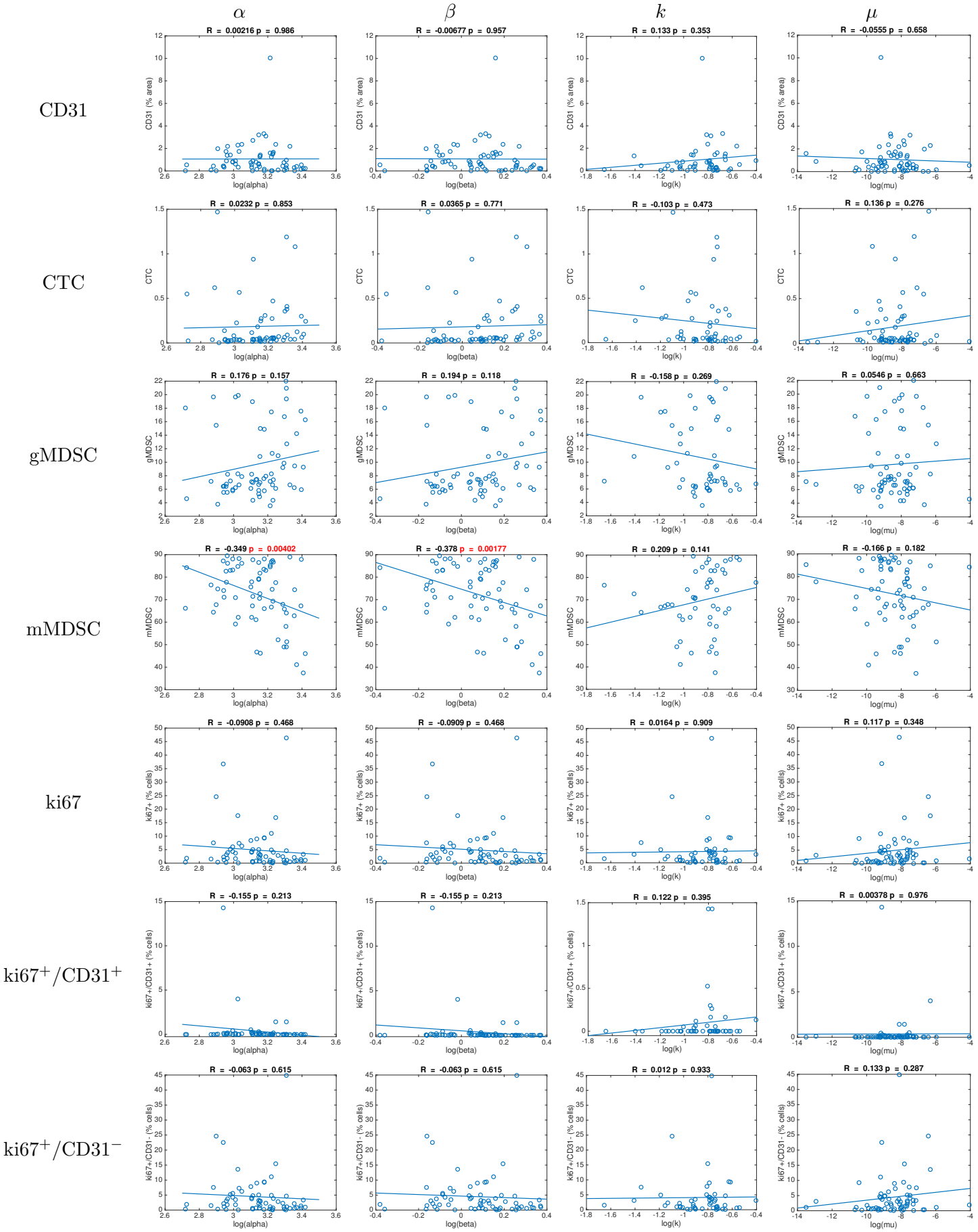

Figure S9. Observed vs Predicted values for the machine learning algorithms

Models for predicting μ

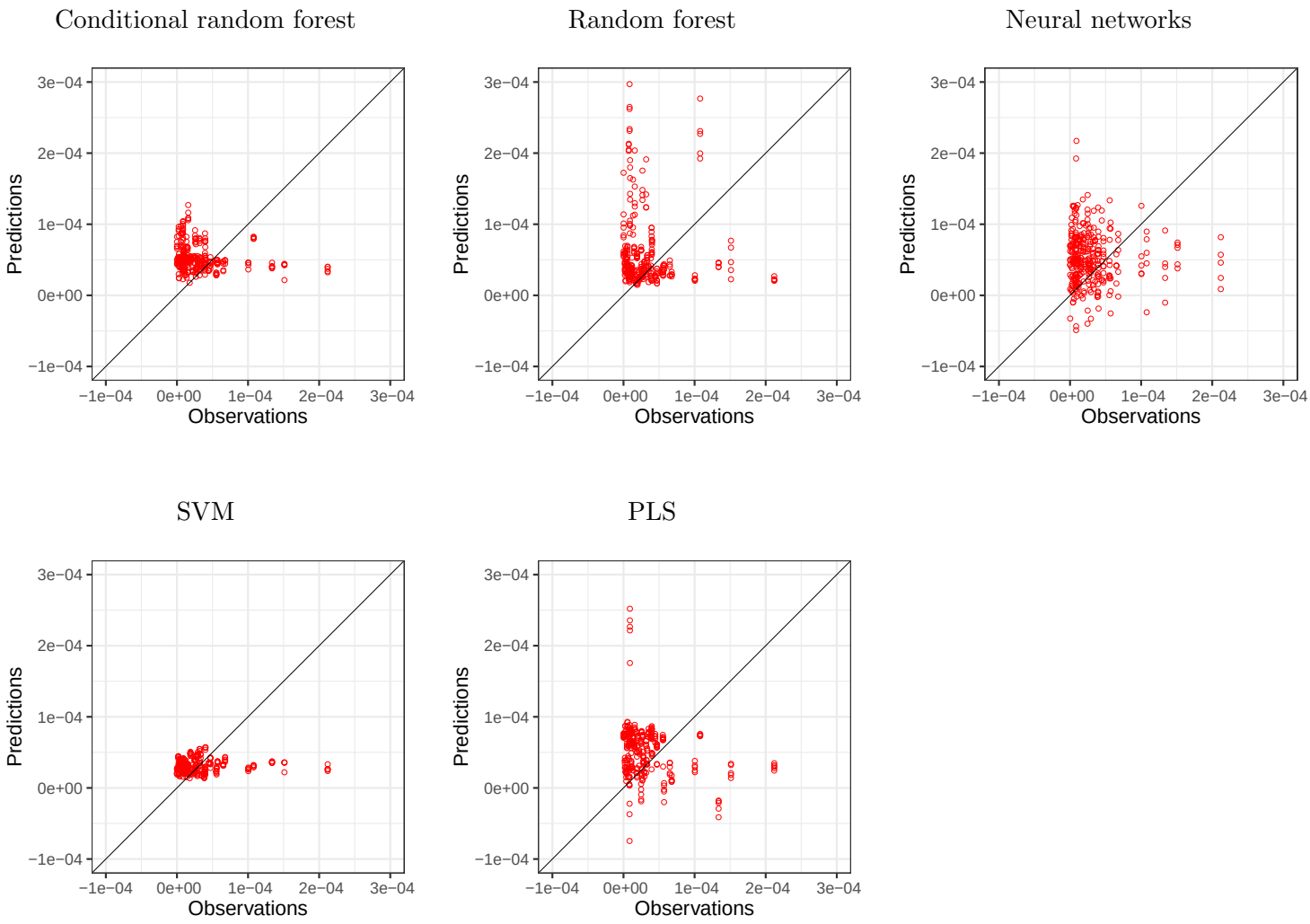

Models for predicting $\log(\mu)$

Conditional random forest

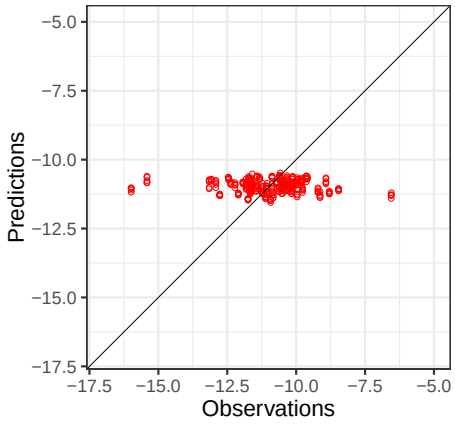

Random forest

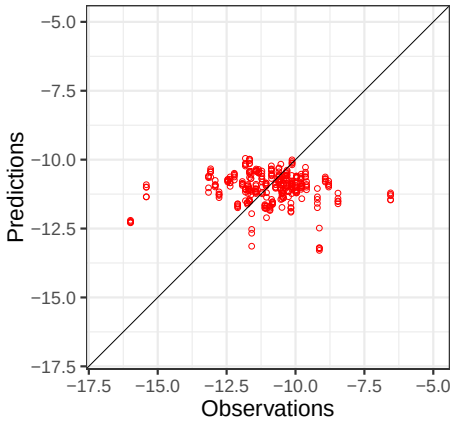

Neural networks

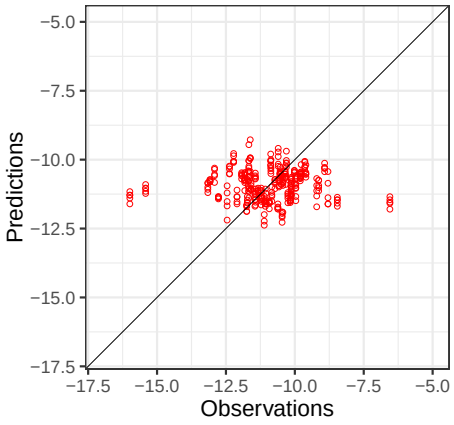

SVM

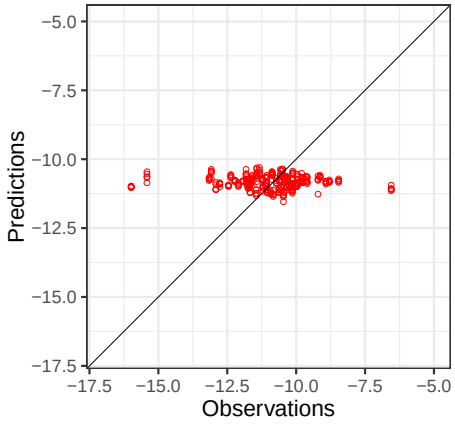

PLS